Article

Developmental Cell

Competition for endothelial cell polarity drives vascular morphogenesis in the mouse retina

Graphical abstract

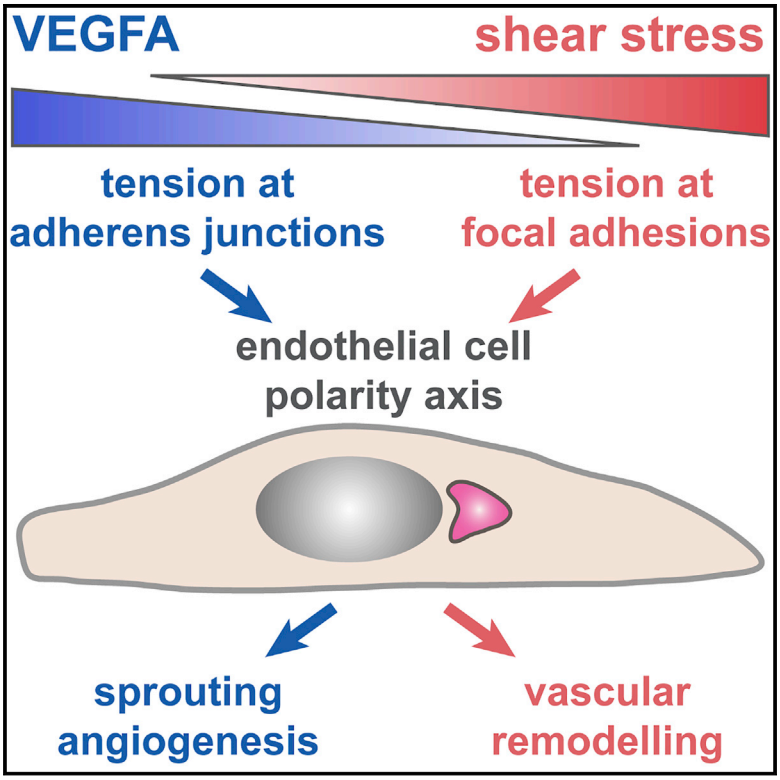

Authors

Pedro Barbacena, Maria Dominguez-Cejudo, Catarina G. Fonseca, ..., Anne Eichmann, Miguel O. Bernabeu, Cláudio A. Franco

Correspondence

cfranco@medicina.ulisboa.pt

In brief

Barbacena and Dominguez-Cejudo et al. demonstrate that shear stress and VEGFA compete to establish the polarization axis of endothelial cells, using the mouse retina as a model. This competition regulates the transition from the sprouting angiogenesis program toward vascular remodeling, thus promoting significant morphological and functional changes in blood vessels.

Highlights

- EC polarity patterns define the sprouting to remodeling (S>R) transition
- Blood flow and VEGFA compete to establish EC polarization patterns in the mouse retina
- Blood flow and VEGFA regulate EC polarity using distinct mechanosensitive complexes

Barbacena et al., 2022, Developmental Cell *57*, 2321–2333
October 10, 2022
https://doi.org/10.1016/j.devcel.2022.09.002

CellPress

Developmental Cell

CellPress
OPEN ACCESS

Article

Competition for endothelial cell polarity drives vascular morphogenesis in the mouse retina

Pedro Barbacena,[1,14] Maria Dominguez-Cejudo,[1,14] Catarina G. Fonseca,[1] Manuel Gómez-González,[2] Laura M. Faure,[2] Georgia Zarkada,[3] Andreia Pena,[1] Anna Pezzarossa,[1,4] Daniela Ramalho,[1] Ylenia Giarratano,[5] Marie Ouarné,[1] David Barata,[1] Isabela C. Fortunato,[1] Lenka Henao Misikova,[1] Ian Mauldin,[5,6] Yulia Carvalho,[1] Xavier Trepat,[2,7,8,9] Pere Roca-Cusachs,[2,8] Anne Eichmann,[3,10,11] Miguel O. Bernabeu,[5,12] and Cláudio A. Franco[1,13,15,*]

[1]Instituto de Medicina Molecular João Lobo Antunes, Faculdade de Medicina, Universidade de Lisboa, Lisbon, Portugal
[2]Institute for Bioengineering of Catalonia (IBEC), the Barcelona Institute of Technology (BIST), Barcelona, Spain
[3]Cardiovascular Research Center, Department of Internal Medicine, Yale University School of Medicine, New Haven, CT, USA
[4]Champalimaud Foundation, Champalimaud Research, Lisbon, Portugal
[5]Centre for Medical Informatics, Usher Institute, The University of Edinburgh, Edinburgh, UK
[6]School of Informatics, The University of Edinburgh, Edinburgh, UK
[7]Facultat de Medicina, Universitat de Barcelona, Barcelona, Spain
[8]Institució Catalana de Recerca i Estudis Avançats (ICREA), Barcelona, Spain
[9]Centro de Investigación Biomédica en Red en Bioingeniería, Biomateriales y Nanomedicina (CIBER-BBN), Barcelona, Spain
[10]Department of Cellular and Molecular Physiology, Yale University School of Medicine, New Haven, CT, USA
[11]Université de Paris, PARCC, INSERM, 75006 Paris, France
[12]The Bayes Centre, The University of Edinburgh, Edinburgh, UK
[13]Universidade Católica Portuguesa, Católica Medical School, Católica Biomedical Research Centre, Lisbon, Portugal
[14]These authors contributed equally
[15]Lead contact
*Correspondence: cfranco@medicina.ulisboa.pt
https://doi.org/10.1016/j.devcel.2022.09.002

SUMMARY

Blood-vessel formation generates unique vascular patterns in each individual. The principles governing the apparent stochasticity of this process remain to be elucidated. Using mathematical methods, we find that the transition between two fundamental vascular morphogenetic programs—sprouting angiogenesis and vascular remodeling—is established by a shift of collective front-to-rear polarity of endothelial cells in the mouse retina. We demonstrate that the competition between biochemical (VEGFA) and mechanical (blood-flow-induced shear stress) cues controls this collective polarity shift. Shear stress increases tension at focal adhesions overriding VEGFA-driven collective polarization, which relies on tension at adherens junctions. We propose that vascular morphogenetic cues compete to regulate individual cell polarity and migration through tension shifts that translates into tissue-level emergent behaviors, ultimately leading to uniquely organized vascular patterns.

INTRODUCTION

The blood vascular network is a branched system irrigating all organs in vertebrates, which is fundamental for embryogenesis, physiology, and healing. Dysfunction of this network is associated with multiple diseases, including cancer progression, diabetic retinopathies, and arteriovenous malformations (Potente and Mäkinen, 2017). Major axial vessels are stereotypical and are formed through vasculogenesis (Potente and Mäkinen, 2017). Yet, expansion of this early embryonic network through angiogenesis (Potente and Mäkinen, 2017), seems stochastic because it generates vasculatures with unique patterns, which can be used for biometric identification (Hartung et al., 2012). Angiogenesis involves two distinct morphogenetic processes: (1) Sprouting angiogenesis, which relies on chemoattractants, such as vascular endothelial growth factor A (VEGFA)|: this process expands pre-existing networks through proliferation, migration, and anastomosis of endothelial cells (ECs), and forms immature networks; and (2) vascular remodeling, which relies on blood-flow-induced shear stress|: this process converts immature networks generated by sprouting angiogenesis into hierarchical vascular networks, requiring vessel pruning, arteriovenous differentiation, and vessel specialization (Korn and Augustin, 2015; Potente and Mäkinen, 2017). How ECs shift between these two morphogenetic processes, and which principles govern the formation of well-organized, yet unique, networks remain outstanding questions in vascular biology.

Sprouting and remodeling morphogenetic programs involve dynamic coordination of cell polarity and migration (Fonseca et al., 2020; Korn and Augustin, 2015), which are regulated by

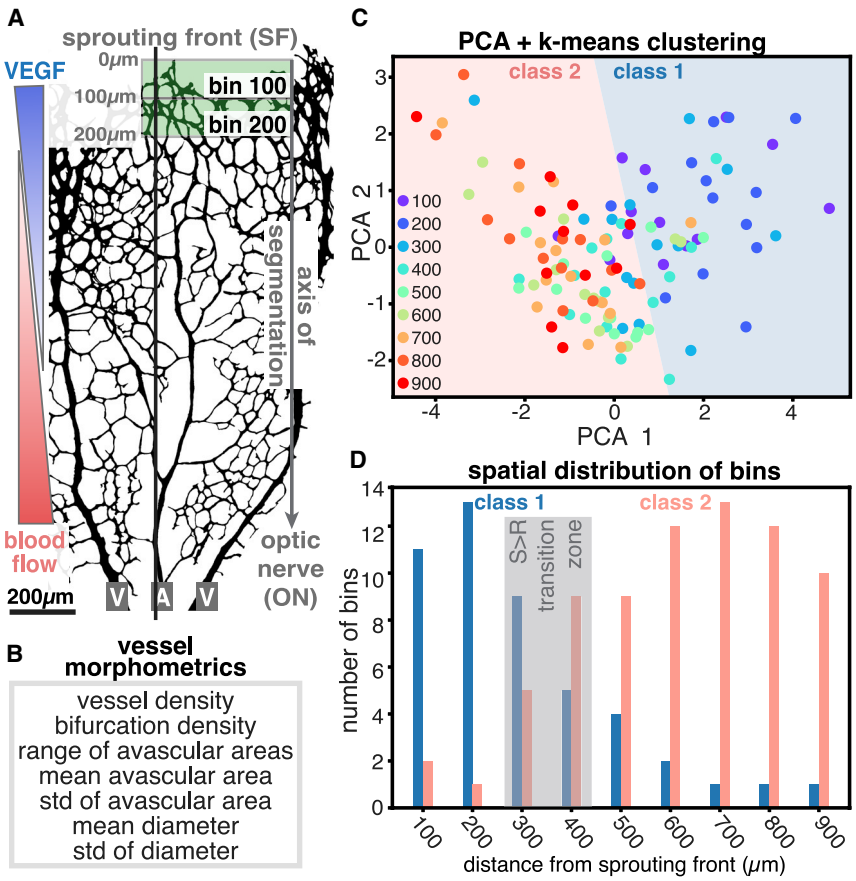

Figure 1. Vessel morphometrics define the morphological S>R transition

(A) Schematic of the sprouting front-to-optic nerve (SF>ON) segmentation axis of the retinal vasculature and its relationship to VEGFA and shear-stress gradients. Segmentation bins 100 and 200 (width 100 μm) are depicted as green rectangles. V, vein; A, artery.

(B) Set of parameters quantified in each bin, termed as vessel morphometrics.

(C) Principal component analysis (PCA) of vessel morphometrics in wild-type vascular networks followed by k-means clustering. Each dot represents one bin in one retina, color coded for the corresponding bin number. k-means clustering identifies 2 classes of objects, class 1 (sprouting) and class 2 (remodeling). n = 14 retinas.

(D) Distribution of the number of class 1 or class 2 bins along the SF>ON axis. Gray rectangle defines the morphological S>R transition zone.

cell-level and tissue-level integration of chemical and mechanical signals. For instance, sprouting angiogenesis involves adherens junction (AJ)-mediated mechanotransduction regulating collective migration downstream of VEGFA stimuli (Cao et al., 2017; Carvalho et al., 2019; Friedl and Mayor, 2017; Hayer et al., 2016). In addition, ECs sense and respond to blood-flow-induced shear stress by aligning, polarizing, and migrating against the flow direction, a phenomenon known as flow-migration coupling (Franco et al., 2015, 2016; Kwon et al., 2016; Park et al., 2021; Tanaka et al., 2021; Tzima et al., 2001). Despite the well-known crosstalk between VEGFA and shear stress to regulate EC sprouting capacity (Chouinard-Pelletier et al., 2013; Ghaffari et al., 2015; Song and Munn, 2011), there is a lack of understanding of how these inputs are integrated at the cell level to shape the vascular network at the tissue scale *in vivo*. Here, we investigated in the mouse retina how chemical (VEGFA) and mechanical (shear-stress) cues interact to promote changes in cellular behaviors underlying the transition between sprouting-to-remodeling morphogenetic programs, which we termed as the S>R transition.

RESULTS

Endothelial polarity patterns define the S>R transition zone

To understand how chemical (VEGFA) and mechanical (shear-stress) cues establish the S>R transition, we analyzed the mouse-retina vasculature, where VEGFA and shear stress are in opposite gradients (Figure 1A). To identify the S>R transition, we first measured 7 vessel morphometric features (Figure S1A) in 100-μm-wide bins along the retina (Figure 1A), following the sprouting front (SF)-to-optic nerve (ON) axis (Figure 1B). Principal component analysis (PCA) classified each bin based on phenotypic similarity (see method details). Each bin point was assigned to one of the two expected biological classes (sprouting or remodeling), using the k-means clustering algorithm (Figure 1C). The frequency distribution of bins from class 1 (sprouting) and class 2 (remodeling) along the SF-to-ON axis determined a transition at 300–400 μm from the SF (Figure 1D), corresponding to a shift in the predominance of class 1 to class 2 bins. Thus, this unbiased quantitative method, based on morphometric features, captured a transition in vascular organization, the morphological S>R transition zone.

Next, we investigated how this morphological transition could be explained at the cellular level, based on chemical and mechanical cues. Sprouting angiogenesis and vascular remodeling rely on EC migration (Fonseca et al., 2020; Korn and Augustin, 2015; Potente and Mäkinen, 2017). EC polarity is a readout for cell migration, and both VEGFA and blood flow induce EC polarization and migration in zebrafish and mouse (Carvalho et al., 2019; Franco et al., 2015; Kwon et al., 2016). Therefore, we hypothesized that changes in EC polarity could underlie the morphological S>R transition. To investigate this interaction, we analyzed the angle between the nucleus-to-Golgi polarity axis and the SF edge (K-angle), or the simulated blood-flow direction (F-angle), for each EC (Figures 2A, S2A, and S2B). The analysis was performed using PolNet (Bernabeu et al., 2018) and applying methods previously established in the lab (Carvalho et al., 2019; Franco et al., 2015, 2016), on the same bins (100 μm wide) used for vessel morphometrics (Figure 1A). At the SF (bin 100 μm), the K-angle centered at ~90° (toward the VEGFA gradient) with a narrow scattering

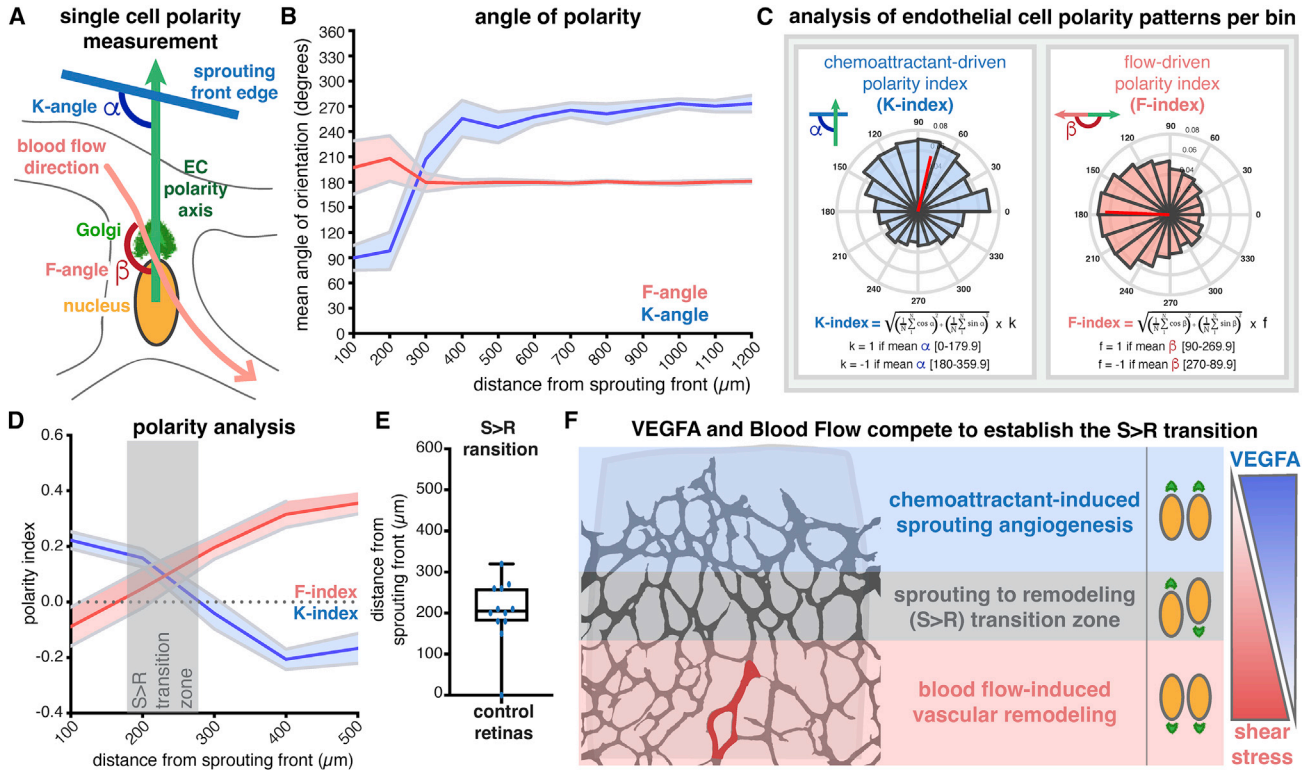

Figure 2. Collective EC polarity patterns establish the cellular S>R transition

(A) Representation of the calculation method for chemoattractant-induced (K-) and flow-induced (F-) angles based on individual EC polarity (nucleus-to-Golgi vector) axis.

(B) Distribution of K-angles (blue) and F-angles (red) along the SF>ON axis. Solid line represents mean, and light area represents SEM.

(C) Calculation of K- and F-indexes, based on K- or F-angles, respectively.

(D) Distribution of K- (blue) and F-indexes (red) within 500 μm from the SF (dashed box in Figure S1C). Solid line represents mean, and light area represents SEM. Dashed black line represents random polarity. Gray rectangle defines the cellular S>R transition zone.

(E) Box plot for the cellular S>R transition in each retina. Whiskers: min. to max.

(F) Morphological annotation of the cellular S>R transition in a mouse retina. Red vessel corresponds to the tip of the retinal artery. n = 11 retinas.

(±14.8°), while the F-angle had a higher dispersion (mean 197.3° ± 31.7°), indicating a poor influence of flow (Figure 2B). At 400 μm away from the SF, blood flow gained a strong influence on EC polarity, with an F-angle centered at 180° with a very narrow dispersion compared with bin 100 μm (~178.8° ± 4.2°; p = 0.0012, Levene test for unequal variances). This was associated with a significant shift for the mean K-angle from ~90° (100 μm) to ~270° (400 μm) (p = 0.0016, Kruskal-Wallis ANOVA test), representing an inversion of polarity from "toward" to "against" the SF (Figures 2B and S2C). From K- and F-angles, we calculated K- and F-indexes, standing for chemoattractant-dependent or flow-dependent polarity indexes (PIs), respectively (Figures 2C and S2D). K- and F-indexes quantify the robustness of EC polarity toward (positive values) or against (negative values) a given polarity cue (details in STAR Methods). Notably, K- and F-indexes are anticorrelated (R^2 = −0.838), highlighting an interdependency between the two polarity cues (Figure S2E). Closer to the SF, the absolute value of the K-index was higher than F-index, demonstrating the dominance of the chemoattractant stimulus (0.22 ± 0.03 versus −0.09 ± 0.07 at 100 μm, respectively) (Figures 2C and S2D). Yet, away from the SF region, K- and F-indexes inverted, with K-indexes becoming negative and lower than F-indexes (−0.21 ± 0.04 versus 0.32 ±0.05 at 400 μm, respectively), demonstrating the dominance of flow in determining EC polarity (Figure 2D). Thus, based on the mathematical description of EC polarity, we defined the cellular S>R transition as a 100-μm-wide region (bin width) centered at the point where the mean F-index intersects the mean of K-index (Figure 2D). The global analysis locates the cellular S>R transition at 230 ± 50 μm from the SF (Figure 2D), while analysis per retina sets it at 203.3 ± 23.0 μm (Figure 2E). Anatomical mapping places the cellular S>R transition just ahead of the artery tip in the mouse retina (Figure 2F). Overall, we propose a system-level mathematical description of EC polarity to predict the S>R transition; that the cellular S>R transition zone (180–280 μm) (Figure 2D) precedes the morphological S>R transition zone (300–400 μm) (Figure 1D); and that the polarity landscape of ECs is dominated by the effect of shear stress, revealing a narrow region of influence for chemoattractant signaling.

Competition between VEGFA and shear stress levels defines the S>R transition zone

Our analysis of the S>R transition predicts that increasing levels of VEGFA or reducing shear stress should promote sprouting

angiogenesis. Conversely, reduction of VEGFA levels or increasing shear-stress levels should promote vascular remodeling. Interestingly, VEGFA and flow have been shown to intersect in *in vitro* studies (Vion et al., 2020). Thus, we manipulated blood flow or VEGFA to disturb the S>R transition. First, we treated animals with captopril (an angiotensin-converting enzyme inhibitor) to reduce blood flow or angiotensin-II to increase blood flow (Nehme et al., 2019). Captopril treatment led to a significant increase in vessel density and in the number of endothelial tip cells, associated with sprouting angiogenesis (Figures 3A and S3A–S3I) and correlated with a spatial shift on the cellular S>R transition from ~230 to ~325 μm (Figure 3B). Angiotensin-II treatment decreased vascular density and the number of tip cells, abolishing the S>R transition zone (Figures 3C, 3D, and S3A–S3I). The apparent lack of transition is likely due to the sensitivity of our method, given the limitations of bin size required for statistical analysis. Therefore, the absence of a clear S>R transition zone should be interpreted as if the transition happens in the first bin. Next, we manipulated VEGFA levels in the mouse retina by intraocular injection of either VEGFA or sFLT1 (a VEGFA inhibitor) (Simons et al., 2016). Similar to captopril, rising VEGFA levels led to an increase in vessel density and the number of tip cells (Figures 3E and S3J–S3R) and shifted the S>R transition from ~230 to ~260 μm (Figure 3F). VEGFA blockage with sFLT1 reduced vascular density, decreased number of tip cells, and abolished the S>R transition (Figures 3G, 3H, and S3J–S3R), similar to angiotensin-II, yet with a stronger effect. These effects were concordant with a trend for increased expression of flow-sensitive genes, Klf2 and Klf4, in angiotensin-II treatment or a decrease in captopril treatment (Figure S4A). These effects also correlated with the distance from the SF where Klf4 protein can be detected in ECs, demonstrating that angiotensin-II and captopril treatments lead to increased or decreased shear-stress levels, respectively (Figures S4B and S4C). The increases and decreases in shear-stress levels were also revealed by an overall increased or decreased PI in capillary ECs, respectively (Figure S3H). Remarkably, drug treatments did not affect endogenous VEGFA-expression levels, suggesting that treatments do not induce significant alterations in tissue-oxygenation levels (Figure S4A).

Analysis of individual retinas confirms statistically significant shifts in the S>R transition zone in all conditions, when compared with control retinas (Figure 3I). Vessel morphometrics analyses (independent of cell polarity) confirmed that captopril and VEGFA led to an enrichment in class 1 (sprouting) bins, whereas angiotensin-II or sFLT1 promoted class 2 (remodeling) bins, when compared with control retinas (Figures 3J, 3K, and S4D). Altogether, these results demonstrate that the cellular S>R transition is established by an interaction between blood-flow (shear-stress) and chemoattractant (VEGFA) gradients, which compete to define EC collective behavior.

Remarkably, excessive VEGFA levels fuel aberrant angiogenesis in pathological conditions, where vessels form immature and poorly functional networks (Fonseca et al., 2020). To test if this competitive behavior between blood flow and chemoattractants could also regulate pathological angiogenesis, we used the oxygen-induced retinopathy (OIR) model as a means to promote aberrant angiogenesis (Scott and Fruttiger, 2010). In this assay, mice are exposed to hyperoxic conditions followed by normoxic conditions. Hyperoxia-induced vascular regression leads to pathological neoangiogenesis posthypoxia (Scott and Fruttiger, 2010), a process dependent on high VEGFA levels (Hollanders et al., 2015). In these conditions, we injected angiotensin-II or captopril from day 4 posthyperoxia for 3 consecutive days and analyzed vascularization of the retina at day 7 posthyperoxia. Captopril treatment enhanced revascularization of the avascular area while angiotensin-II led to a delay in vascularization (Figures 4A and 4B). This suggests that manipulation of flow-migration coupling can influence the outcome of pathological angiogenesis as it does during development.

Mechanotransduction at focal adhesions governs shear-stress-induced polarity

Numerous reports proposed that ECs polarize upstream or downstream in response to flow via different mechanisms (McCue et al., 2006; Tanaka et al., 2021; Tzima et al., 2003), but the mechanism regulating flow-migration coupling remains unclear. Several shear-stress sensors have been identified in ECs, including piezo1, plexinD1, focal adhesions (FAs), the VEGF receptor 2 (VEGFR2)/platelet and endothelial cell adhesion molecule 1 (PECAM1)/VE-cadherin (VEcad) complex, and caveolae (Tanaka et al., 2021; Tzima et al., 2005; Xanthis et al., 2019). To clarify how shear stress promotes EC polarity, we establish *in vitro* flow conditions in which ECs polarize against the flow direction, measured by the PI (Carvalho et al., 2019), in a force-dependent manner (Figures S5A and S5B), as seen *in vivo*. We used 2.0 Pa for 4 h as our standard to induce robust collective polarization of EC monolayers. Flow-dependent EC polarization was associated with significant changes in FAs, as previously reported (Jalali et al., 2001; Li et al., 1997). Exposure to shear stress increased the number of FAs per cell, increased their mean length (Figures 5A, 5B, S5C, and S5D), increased the co-localization of vinculin with integrin alpha 5 (ITGA5) (Figures S5E–S5G) and of phosphorylated paxillin with vinculin (Figures S5H and S5I), and increased the phosphorylation of paxillin, vinculin, focal adhesion kinase (FAK), and protein kinase B (PKB/AKT) (Figures S6A and S6B). Remarkably, shear stress induced a bias in the alignment of both FA morphology and the distribution of vinculin-activated integrin beta 1 (aITGB1) co-localization in the direction of flow (Figures 5C and 5D). Next, we tested the involvement of FAs in EC polarity response. First, we knocked down (KD) either ITGB1, ITGA5, or talin 1, as a means to decrease FAs. However, when applying flow, KD cells readily detached, and measurements were not possible. To circumvent this technical issue, we used RGDS, a peptide that binds to integrin RGD-binding motifs and blocks integrin-mediated adhesion (Kapp et al., 2017). RGDS-treatment impaired FA formation (Figures S6D and S6E) and led to a significant decrease in EC polarization against the flow direction (Figure 5E). Cilengitide, an RGDS-mimic (Kapp et al., 2017), led to a similar effect (Figure 5E). Thus, FAs are necessary for flow-induced EC polarity.

FAs regulate translation-dependent and translation-independent cellular responses. Given that inhibition of transcription using triptolide, or translation using puromycin, did not affect flow-mediated polarization (Figures S6F and S6G) thus polarity response is translation-independent. FAs are mechanoresponsive, sensing the rigidity, molecular composition, and

CellPress
OPEN ACCESS

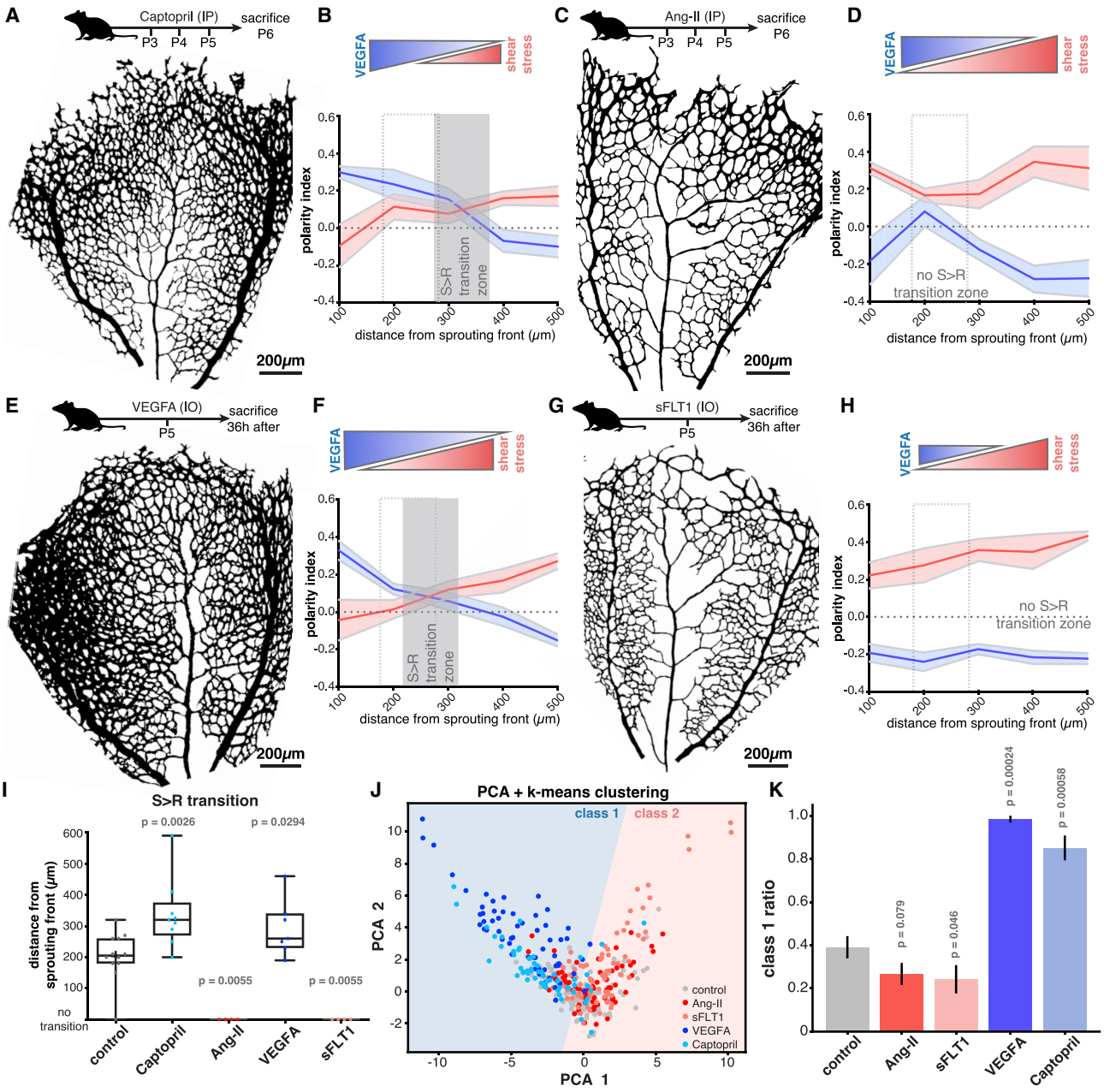

Figure 3. VEGFA and flow pattern govern the S>R transition

(A, C, E, and G) Top: scheme of designated compound injection and collection of samples; Bottom: representative image of the vascular network following designated compound treatment.

(B, D, F, and H) Top: predicted strength of each morphogen based on designated compound treatment. Bottom: distribution of K- (blue) and F- (red) indexes within 500 μm of the SF. Solid line represents mean, and light area represents SEM. Dashed gray line represents random polarity. Gray rectangle defines each compound-treated S>R transition. Dashed gray bounding rectangle shows control S>R transition (defined in Figure 2D).

(I) Box plot for the cellular S>R transition in each retina of control, captopril, angiotensin-II, VEGFA and sFLT1 retinas. n = 11 control; n = 9 captopril; n = 4 angiotensin II; n = 7 VEGFA; n = 4 sFLT1. p values from Mann-Whitney test between control and the corresponding group. Whiskers: min. to max.

(J) k-means clustering analysis of vessel morphometrics for designated conditions projected into the binary PCA clustering space defined in Figure 1C. Each dot represents one bin for each retina.

(K) Ratio of class 1 bins over total bins for designated conditions. n = 14 control; n = 9 captopril; n = 8 angiotensin II; n = 7 VEGFA; n = 9 sFLT1. p values of a two-tailed Mann-Whitney test between control and the corresponding group. Error bars: SEM.

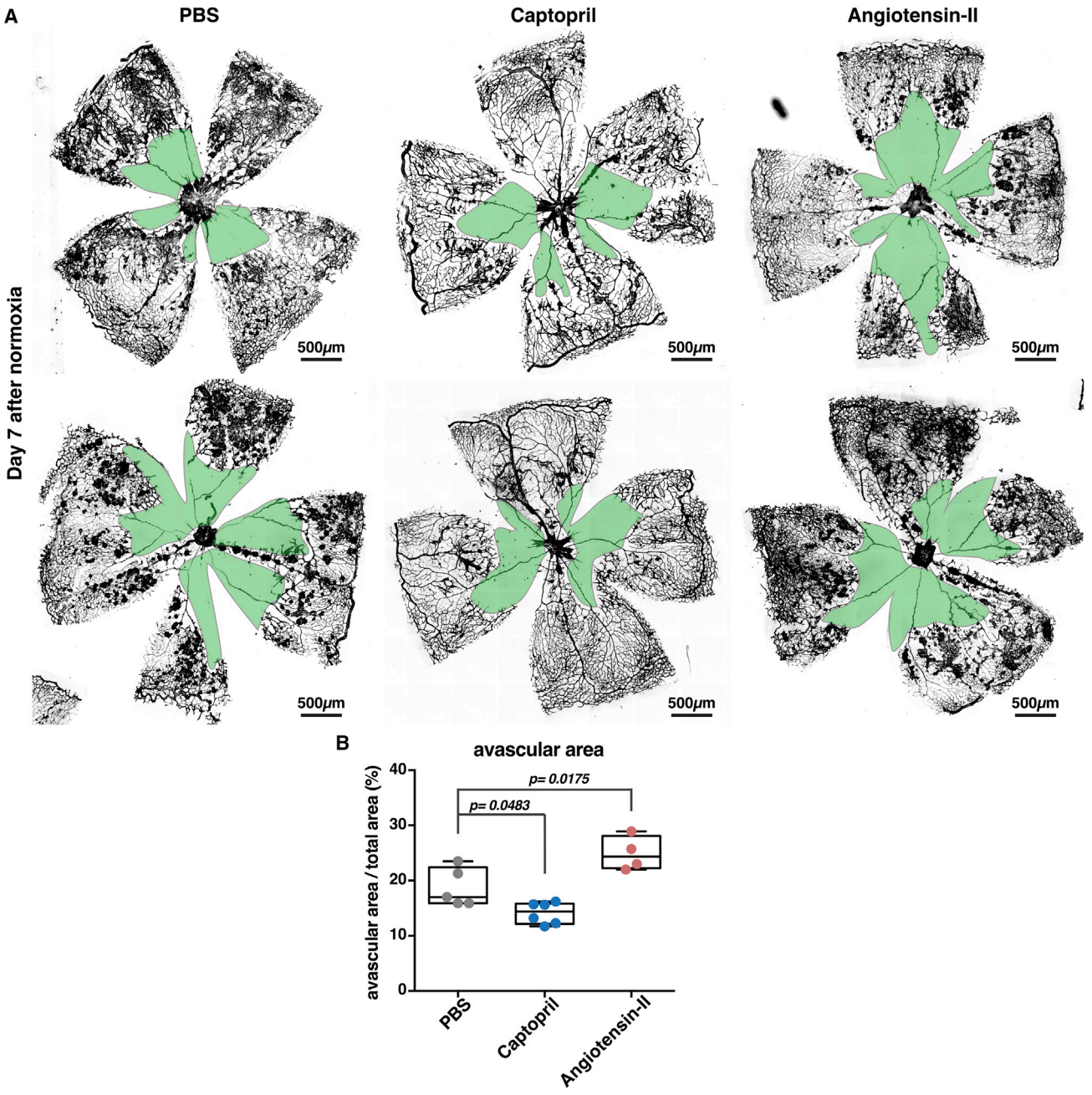

Figure 4. Effects of captopril and angiotensin-II in pathological angiogenesis

(A) Representative images of OIR-exposed mouse retinas at 7 days after return to normoxia treated with PBS, captopril or, angiotensin-II in days 4, 5, and 6. Retinas were stained for CD31 (gray) and avascular areas are highlighted in green.

(B) Quantification of fraction of avascular area over total area for designated treatments. PBS (n = 5), captopril (n = 6), and angiotensin-II (n = 4) mouse retinas. p values from one-way ANOVA with Tukey multiple-comparisons tests. Whiskers: min. to max.

conformation of the extracellular matrix (ECM) (Kechagia et al., 2019). To test if mechanotransduction regulates shear-stress-induced polarity responses, we manipulated substrate stiffness. The range of young modulus for vascular basement membranes *in vivo* have been proposed to be in the range of 1 kPa–1 MPa (Leclech et al., 2020; Wood et al., 2010). Flow-stimulated human umbilical vein ECs (HUVECs) seeded on 3 or 18 kPa soft polydimethylsiloxane (PDMS) had bigger FAs than in static conditions (Figure S7A). Interestingly, shear stress-stimulated ECs at 3 kPa showed a tendency for fewer FAs and a lower PI compared with those at 18 kPa (Figures S7A and S7B). The relationship between stiffness and flow-induced PI was even more evident in stiffer substrates. Stiffer hard PDMS (1 MPa) had higher PIs compared with softer hard PDMS (280 kPa), a phenomenon that was positively associated with the length of FAs in the different conditions (Figures S7C and S7D). These results suggest that the ability of

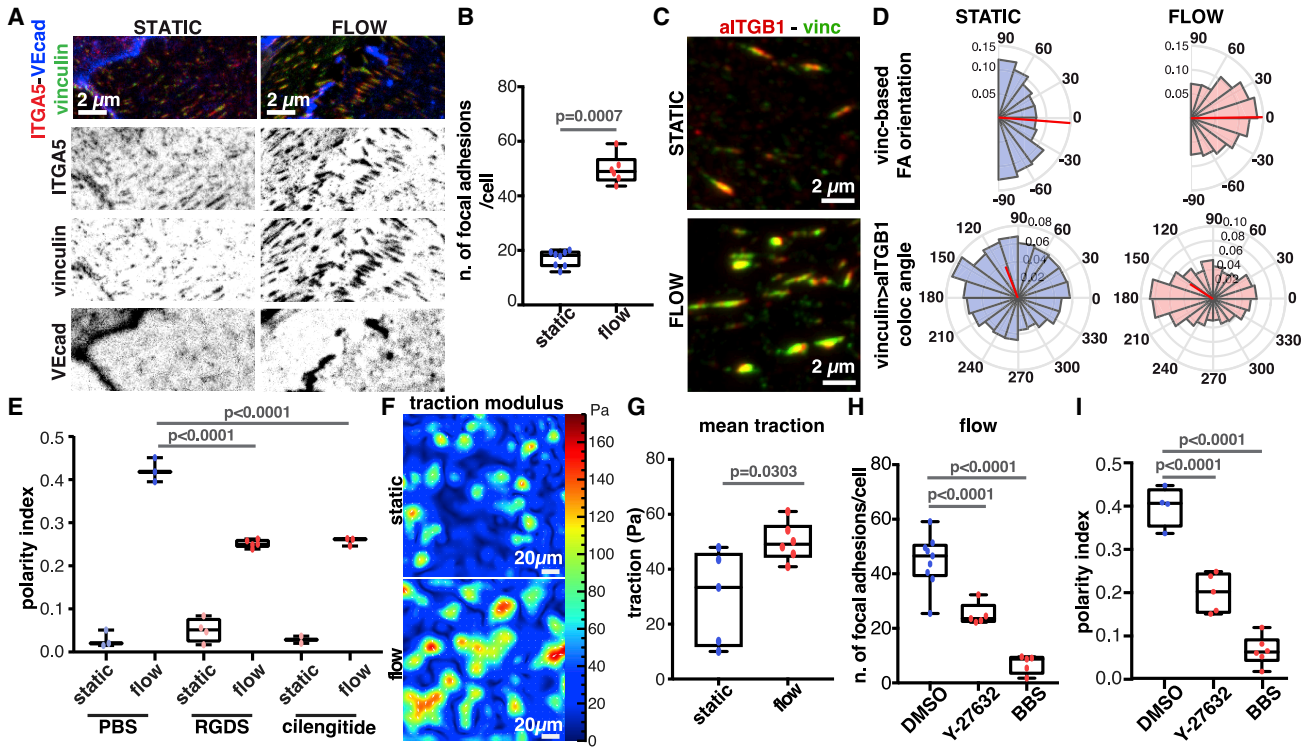

Figure 5. FA-mediated traction forces drive flow-induced polarity

(A) Representative image of AJs (VE-cadherin [VEcad], blue) and FAs (vinculin [green] and ITGA5 (red) in static or flow-stimulated HUVEC monolayers (high magnification from Figure S5C).

(B) Box plot for the number of FAs in static or flow conditions. n = 8 (static) and n = 6 (flow). p value from Mann-Whitney test. Whiskers: min. to max.

(C) Representative super-resolution image of co-localization between vinculin (green) and activated integrin beta 1 (aITGB1) (red) in static or flow-stimulated HUVEC monolayers. Scale bars: 2 μm.

(D) Top: angular histograms for the distribution of vinculin FA orientation in static and flow conditions. Bottom: mean angle of orientation of the vector from vinculin to aITGB1 centroids in relation to right-to-left slide axis in static and flow conditions. Flow direction is right to left. n = 20 images from 4 separate experiments.

(E) Box plot for polarity index in static or flow-stimulated HUVEC monolayers treated with PBS (n = 3), RGDS (n = 5), and cilengitide (n = 3), p values from one-way ANOVA with Sidak test. Whiskers: min. to max.

(F and G) Mean traction maps (F) and box plot of mean traction forces (G) exerted by static or flow-stimulated HUVEC monolayers. n = 4 static; n = 5 flow. p values from Mann-Whitney test. Whiskers: min. to max.

(H) Box plot for numbers of focal adhesions in flow-stimulated HUVEC monolayers treated with DMSO (n = 9), Y-27632 (n = 5), or BBS (blebbistatin, n = 5). p values from Mann-Whitney test. Whiskers: min. to max.

(I) Box plot of polarity index in static or flow-stimulated HUVEC monolayers treated with DMSO (n = 4), Y-27632 (n = 5) or BBS (blebbistatin, n = 6). p values from one-way ANOVA with Sidak test. Whiskers: min. to max.

ECs to polarize against the flow direction is dependent on the strength of adhesion to the ECM. To confirm this hypothesis, we measured FA-mediated tension through traction force microscopy (TFM) (Butler et al., 2002). As expected, direct application of flow on the substrate without cells does not generate measurable tractions (Figures S7E and S7F). TFM revealed that flow-stimulated ECs exerted significantly higher levels of traction forces on the substrate, when compared with static conditions (Figures 5F and 5G). However, the amount of tension per vinculin molecule, estimated by FRET efficiency, was similar under both flow and static conditions (Figures S7G and S7H). FA maturation and traction forces are mediated by myosin-II-dependent contractility (Chrzanowska-Wodnicka and Burridge, 1996). Inhibition of both Rho-associated protein kinase (ROCK) (Y-27632) and myosin ATPase activity (blebbistatin [BBS]) led to a significant decrease in the number and size of FAs (Figures 5H, S7I, and S7J), and in the co-localization of vinculin with ITGA5 (Figure S7K), which was associated with a decrease in traction forces, when compared with control conditions (compare Figures 5F and 5G with Figures S7L and S7M). These effects correlated with a significant impairment in flow-induced EC polarization under actomyosin inhibition (Figure 5I). Thus, our data suggest that shear stress stimulates FA assembly and enhances traction forces, which are required for flow-induced EC polarization.

A shift in tension distribution regulates the competition between chemoattractants and shear stress to establish EC polarity patterns

Previous reports demonstrated that collective EC polarity driven by chemoattractants involves tension at AJs (Carvalho et al., 2019; Hayer et al., 2016; Huveneers et al., 2012), while our data revealed that flow-mediated polarity is induced through tension at FAs (Figure 6A). Thus, we hypothesize that blood flow and chemoattractants might compete for EC polarity by shifting the

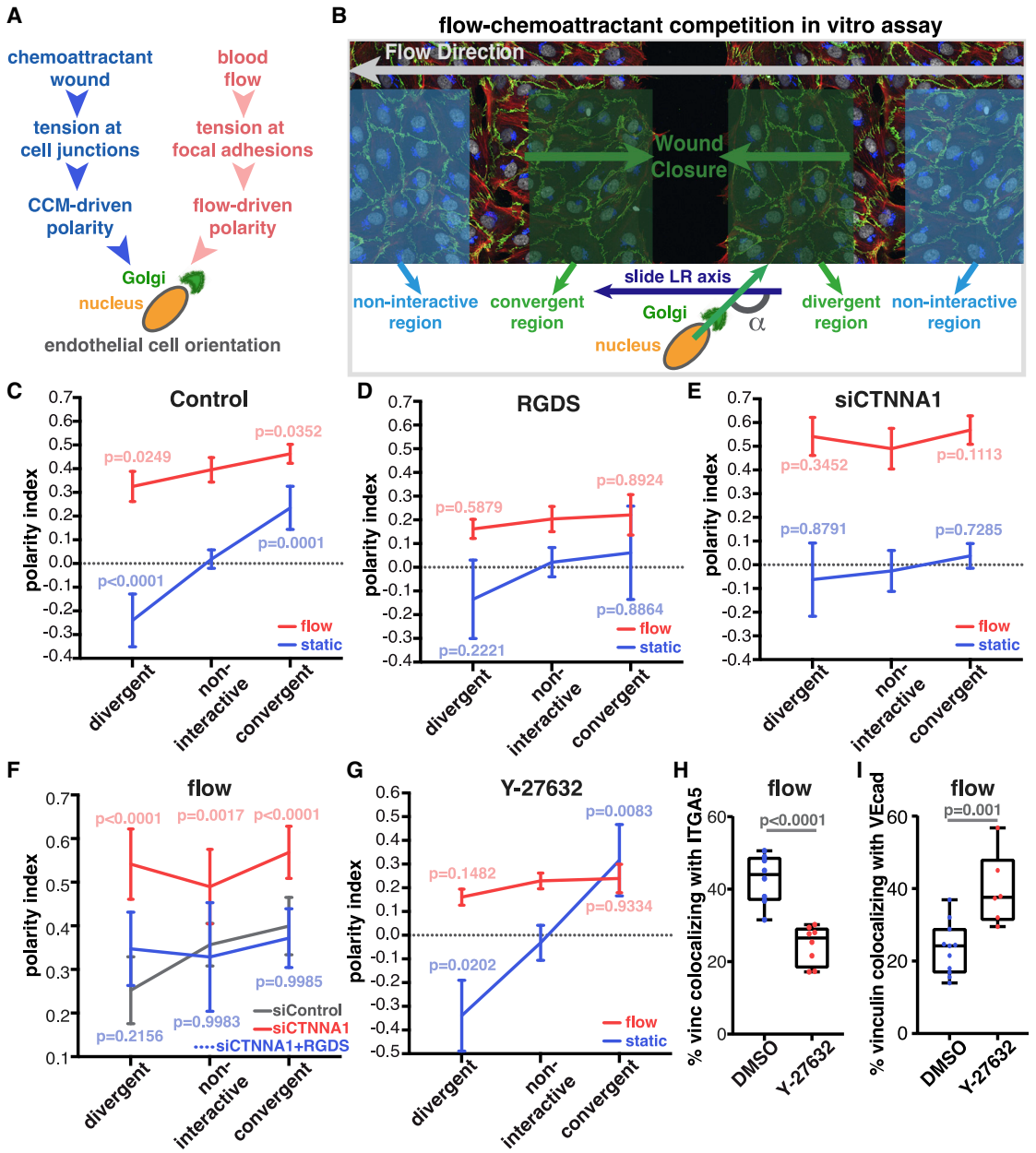

Figure 6. Chemoattractants and blood flow compete to establish the main polarity axis of ECs

(A) Schematic of proposed model for chemoattractant- and flow-induced collective polarity of ECs.

(B) Layout of the flow-chemoattractant competition *in vitro* assay depicting the relationship between each wound side and the flow direction. EC polarity angle (α) is measured in relation to the right-to-left (RL) axis of the slide, in the same direction of flow.

(C–E) PI for designated regions in static (blue) or flow (red) in control (C), RGDS (D) and siCTNNA1 (E) HUVECs. n = 4 control; n = 5 RGDS; n = 7 siCTNNA1. p values for multiple comparisons with noninteractive region one-way ANOVA with Sidak test. Error bars: SD.

(F) PI for designated regions in static or flow conditions in si-control (red) or siCTNNA1 HUVECs treated with PBS (gray) or RGDS (blue). n = 4 per condition; red p values (siCTNNA1) and blue p values (siCTNNA1 + RGDS) for multiple comparisons with si-control one-way ANOVA with Sidak test. Error bars: SD.

(G) PI for designated regions in static (blue) or flow (red) conditions in HUVECs treated with DMSO or Y-27632. n = 5 per condition. p values correspond to multiple comparisons with noninteractive region one-way ANOVA with Sidak test. Error bars: SD.

(H) Box plot for percentage for vinculin colocalizing with in ITGA5 in flow-stimulated DMSO- or Y-27632-treated HUVEC monolayers. n = 8 per condition. p values from Mann-Whitney test. Whiskers: min. to max.

(I) Box plot of percentage of vinculin colocalizing with VE-cadherin (VEcad) in flow-stimulated HUVEC monolayers treated with DMSO (n = 11) or Y-27632 (n = 6). p values from Mann-Whitney test. Whiskers: min. to max.

balance of tension at these different mechanosensitive complexes. To experimentally test this hypothesis, we established an *in vitro* assay in which wounded HUVEC monolayers are exposed or not exposed to flow (Figure 6B). The wound in the monolayer generates a free edge that stimulates collective migration similarly to chemoattractants (Carvalho et al., 2019; Friedl and Mayor, 2017; Vitorino and Meyer, 2008). We used the scratch-wound assay rather than VEGFA gradients because countergradients of soluble factors are difficult to establish under a high flow rate (20 mL/min) conditions. KD of VEGFR2-inhibited free edge induced polarity while not affecting flow-induced polarity (Figures S8A and S8B), confirming that the scratch-wound assay is a suitable surrogate to investigate chemoattractant-induced polarity. In this competition assay, we determined the PIs of ECs in ~200-μm wide regions on the left (convergent), on the right (divergent), and in regions >2 mm away (noninteractive) from the wound (Figure 6B). Under static conditions, ECs were unpolarized (PI = ~0.0) in noninteractive regions, while convergent and divergent regions had mirrored responses (PIs of 0.23 and −0.24, respectively) (Figure 6C). Shear stress (2.0 Pa) induced robust EC polarity in all the regions (Figure 6C), suggesting that shear stress is a stronger polarity cue than the free edge. Yet, instead of a homogeneous flow response, we observed a statistically significant lower PI (0.33) in divergent compared with noninteractive regions (0.39), which was also significantly lower than in the convergent region (0.46) (Figure 6C). These results suggest that each polarity cue triggers independent pathways, which can lead to competitive or cooperative effects on cell polarity depending on the directionality of each polarity cue.

Next, we perturbed FAs and AJs and tested their effects in the competition assay. Inhibition of FA formation, through RGDS treatment, disrupted free-edge- and flow-induced EC polarity, when compared with control cells (compare Figure 6C and Figure 6D). siRNA-mediated KD of alpha-catenin (siCTNNA1) (Figure S8C), a crucial protein of AJs (Bazellières et al., 2015), led to the expected inhibition of free edge-induced polarity in static conditions (Figure 6E), but, surprisingly, also led to a significant sensitization to shear stress when compared with si-control cells (Figures 6E and S8D). This effect was further confirmed by KD of VEcad (siCDH5) (Figure S8E); siRNA-mediated depletion of PECAM1 or VEGFR2 demonstrate that AJs regulate flow-induced EC polarization independently of the well-known VEcad-PECAM1-VEGFR2 mechanosensory complex (Tzima et al., 2005; Figures S8B and S8F). Together, these results suggest that AJs are positive regulators of free edge-induced polarization and negative regulators of flow-induced polarization.

Mechanical feedback between AJ- and FA-based adhesion has been previously documented (Hur et al., 2012; Liu et al., 2010; Mertz et al., 2013; Tambe et al., 2011). Thus, we hypothesized that disruption of AJs could stimulate flow-dependent polarization by promoting FA-dependent mechanotransduction. Supporting this possibility, we observed that siCTNNA1 cells have more and larger FAs than control cells in static and flow conditions (Figures S8G–S8I). In agreement, inhibition of FAs in siCTNNA1 cells with RGDS led to a significant reduction of flow-mediated polarity, to levels indistinguishable from si-control cells (Figure 6F). Vinculin is a protein known to be recruited to both FAs and AJs in a force-dependent manner (Bays and DeMali, 2017). In agreement with higher traction forces on FAs under flow conditions (Figure 5), shear stress significantly increased vinculin co-localization with FAs (Figure S8J) and led to a significant decrease in co-localization with AJs (Figure S18K). This suggests a shift in the distribution of mechanical stresses upon flow exposure. In agreement, siCTNNA1 cells display an increase in co-localization of vinculin with ITGA5 in static conditions, while no significant changes were observed under flow (Figure S8J). Remarkably, monolayer stress microscopy (Tambe et al., 2011) demonstrated that intercellular tension was increased upon flow exposure, in accordance with a previous report (Hur et al., 2012; Figures S8M and S8N). This result was somewhat surprising when considering the shift in vinculin co-localization with FAs and AJs, yet it suggests that the overall increase in clustered vinculin (Figures 5 and S5) detected in the co-localization analysis is preferentially bound to FAs rather than to AJs. Taken together, these observations suggest that flow promotes tension both at FAs and AJs, but that flow-dependent tension at FAs is a stronger polarity stimulus than tension at AJs, a response that is further enhanced when AJs are disrupted. In accordance, inhibition of actomyosin contractility by Y-27632 negatively regulated flow-induced polarity in divergent, noninteractive and convergent regions (Figure 6G). Yet, Y-27632 did not significantly alter free-edge-induced polarity ($p = 0.1208$ in divergent; $p = 0.7594$ in noninteractive; $p = 0.2168$ in convergent—compare Figures 6C and 6G. The effect of Y-27632 on PIs correlated with a decrease in the co-localization between vinculin and ITGA5 (Figure 6H) and an increase in the co-localization of vinculin with VEcad under flow conditions (Figure 6I). Taken together, these observations strongly suggest that shear stress increases ROCK-dependent FA-derived polarity cues and reduces the ability of cells to coordinate free edge collective behaviors that rely on tension at AJs.

Next, we sought to integrate these *in vitro* observations into the physiological context of angiogenesis by manipulating tension at FAs and AJs and to measure their effects on the S>R transition. Inhibition of ROCK-induced actomyosin contractility decreased integrin-mediated binding to the ECM, as shown by a marked decrease of phosphorylated PAX (pPAX) staining in invading tip cells (Figure S9A), and resulted in a significantly delayed the S>R transition zone (Figures 7A, S9B, and S9C), similarly to *in vitro* (Figure 6G). These results were further confirmed using an endothelial-specific deletion of Myh9, coding for the heavy chain of the myosin-IIA. Myh9 EC-KO showed a strong decrease in pPAX staining (Figure S9D) but no major change in VEcad intensity levels (Figure S9E), as previously reported (Figueiredo et al., 2021), which correlated with a decrease in flow-induced polarity and a delay in the S>R transition (Figures 7B, S9F, and S9G). This delay was consistent with an increase on the distance from the SF for the presence of Klf4-positive ECs (Figures S10A–S10C). Yet Myh9 EC-KO showed elevated retinal VEGFA levels that could also impact on the S>R transition (Figure S10A). To disrupt AJ-mediated tension, we performed endothelial-specific deletion of Ctnna1 *in vivo*. Ctnna1 EC-KO showed decreased and disrupted VEcad staining in mouse retina, but no changes in pPAX intensity were detected (Figures S9H and S9I). Deletion of Ctnna1 in ECs promoted flow-dependent polarity while inhibiting chemoattractant-induced polarity (Figures 7C, S9J, and S9K). In accordance,

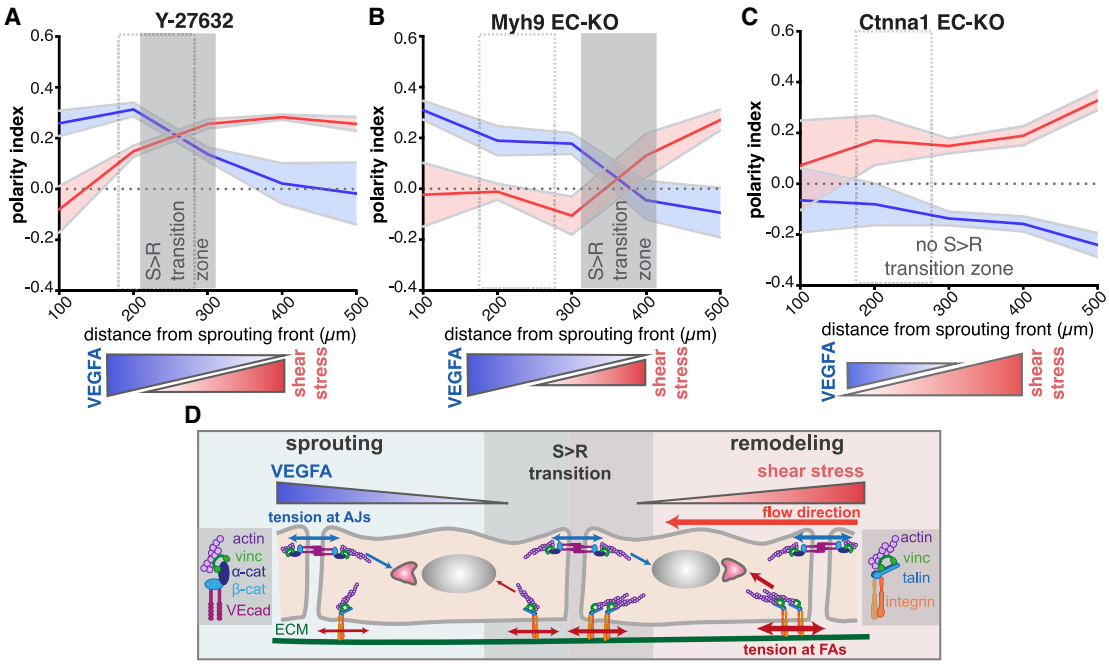

Figure 7. Manipulation of AJs or FAs alters the S>R transition zone

(A–C) Top: distribution of K- (blue) and F- (red) indexes within 500 μm of the SF. Bottom: predicted strength of each morphogen based on designated drug treatment or KO animal. Solid line represents mean, and light area represents SEM. Dashed gray line represents random polarity. Gray rectangle defines each drug-treated or KO animal's S>R transition. Dashed gray bounding rectangle shows control S>R transition (defined in Figure 2D). n = 5 Y-27632; n = 5 Myh9 EC-KO; n = 4. Ctnna1 EC-KO, arterial regions.

(D) Schematic representation of the biomechanical regulation of the S>R transition.

Klf4-positive ECs were found to be closer to the SF when compared with control retinas (Figures S10D and S10E).

Analysis of individual retinas confirms statistically significant shifts in the S>R transition zone in all conditions, when compared with control retinas (Figure S9L).

Taken together, we propose a theoretical model for the establishment of the S>R transition zone based on the gradual increase of flow-mediated tension at FAs, which promotes a shift from AJ-mediated polarity toward FA-mediated polarity (Figure 7D).

DISCUSSION

Here we propose that the competitive regulation of cell polarity leads to a shift in cell-level migratory behavior (toward VEGFA or against blood flow), which translates into a tissue-level morphogenetic event, the S>R transition. This simple principle enables local vascular adaptation that could underlie the generation of unique vascular patterns. Our analysis focused on arteries as the gradients of flow and VEGFA, which are oriented as opposite gradients, thus interacting in a competitive way. However, the same interaction between flow and VEGFA also occurs ahead of veins, and the distribution of flow patterns becomes more intricate and difficult to analyze. Yet, in veins, the gradients of shear stress and VEGFA are not in opposite directions, which correlates well with a lower remodeling of the vascular network ahead of veins. As VEGFA levels and flow patterns differ in each organ during development and in pathological conditions, our model could provide a biological explanation for organotypic vasculature and why these patterns become disrupted in disease (Augustin and Koh, 2017).

We have identified the S>R transition based on cell polarity, which could be explained largely from a biomechanical perspective. Nevertheless, shear-stress levels and pressure differences does also influence gene expression, cell identity, and sprouting activity of ECs (Chouinard-Pelletier et al., 2013; Ghaffari et al., 2015; Song and Munn, 2011).

Moreover, besides VEGFA, several other signaling molecules further regulate vascular biology, such as bone morphogenetic protein (BMP)9/10, NOTCH, sphingosine 1-phosphate (S1P), and angiopoietin 2 (Potente and Mäkinen, 2017). Thus, our current model and methods could be powerful tools to explore the interconnections between mechanical and biochemical signaling leading to a better refinement of our understanding of vascular morphogenesis. In this context, one interesting biological process is arteriogenesis, in which prearterial ECs differentiate at the SF and migrate upstream to contribute to artery formation (Hasan et al., 2017; Pitulescu et al., 2017; Su et al., 2018). Our *in vitro* and *in vivo* observations are based on quantitative analysis of collective polarity patterns of ECs. This implies that flow-migration coupling is a universal feature of ECs, thus suggesting the hypothesis that prearterial cells are more efficient in this process than surrounding cells. Determining if and how prearterial ECs are more effective at flow-migration coupling than neighboring ECs can have important implications for vascular morphogenesis. NOTCH, CXCR4,and BMP signaling have been linked to arteriogenesis and/or to modulate EC shear-stress responses (Baeyens et al., 2015; Cartier and Hla, 2019; Mack et al., 2017;

Tanaka et al., 2021) and thus are prime candidates to fine-tune the S>R transition at the single-cell level. Moreover, computational modeling of adaptation and maladaptation showed that well-organized vascular networks rely on tight feedback between vessel caliber control and hemodynamics (Alberding and Secomb, 2021; Pries et al., 2009) and the transfer of information from distal to proximal vessels in arteries (Pries et al., 2010). How these flows of information relate to EC polarity and the S>R transition remains to be explored.

Excessive VEGFA levels fuel pathological angiogenesis, which is characterized by immature and poorly functioning networks. Remarkably, normalization of the tumor vasculature is therapeutically beneficial and can be achieved by decreasing VEGFA signaling (Carmeliet and Jain, 2011; Jain, 2001). Intriguingly, vessel normalization can also be achieved by increasing blood flow through physical exercise (Schadler et al., 2016). Most normalization strategies are linked to vessel regression, generally associated with EC apoptosis (Martin et al., 2019). Our results in the OIR model suggest an alternative mechanism. We envisage that VEGFA inhibition or blood-flow enhancement could both promote vascular organization through vascular remodeling by enabling flow-mediated cell polarity and migration.

Investigating the competitive and synergistic interactions driving cell polarity and the interplay between biochemical and physical crosstalk could offer opportunities to modulate the S>R transition and regulate vascular morphogenesis in health and disease.

Limitations of the study

This study was conducted using the mouse retina as a well-characterized model of angiogenesis. Yet it remains a specialized neurovascular bed, and it is not a surrogate for all angiogenic processes, including pathological conditions such as tumor angiogenesis. Thus, further studies are required to evaluate the overall generalization on the conclusions of this study. Another limitation lies on the control of hemodynamic conditions using pharmacological approaches. Our experimental model does not allow for direct measurements of flow velocity or shear stress levels. Therefore, a level of uncertainty regarding the extent of shear stress alterations upon captopril and angiotensin-II injection *in vivo* remain. A final limitation of this study lies on the bin size (100 μm) required to measure the PI for ECs *in vivo*. Calculation of a PI requires a substantial number of ECs, which limits the spatial resolution of this study. In addition, a PI only captures group dynamics, and it does not evaluate individual cell behavior.

STAR★METHODS

Detailed methods are provided in the online version of this paper and include the following:

- KEY RESOURCES TABLE
- RESOURCE AVAILABILITY
  - Lead contact
  - Materials availability
  - Data and code availability
- EXPERIMENTAL MODEL AND SUBJECT DETAILS
  - Mice
  - Ethics statement
  - Culture of HUVECs
- METHOD DETAILS
  - *In vivo* mouse treatments
  - Viral production and transduction
  - Immunofluorescence on mouse retinas
  - siRNA transfection
  - Flow microfluidic assays
  - Drugs assays
  - Immunofluorescence of cultured HUVECs
  - Protein extraction and western blotting
  - RNA extraction and cDNA synthesis
  - RT-qPCR
  - PDMS gels
  - Traction force microscopy and monolayer stress microscopy
  - Proximity ligation assay
- QUANTIFICATION AND STATISTICAL ANALYSIS
  - Tension sensor FRET measurements
  - Quantification of Focal Adhesions and Colocalization Analysis
  - Analysis of adhesion orientation and vinculin-aITGB1 colocalization angle
  - Vessel and endothelial density analysis
  - Vascular morphogenesis parameters and principal component analysis
  - Polarity index quantifications *in vitro*
  - Flow and chemoattractant polarity indexes in retinas
  - Statistical analysis

SUPPLEMENTAL INFORMATION

Supplemental information can be found online at https://doi.org/10.1016/j.devcel.2022.09.002.

ACKNOWLEDGMENTS

We thank the VML lab and Foundation Leducq ATTRACT members for helpful discussions. We thank Isabel Flores for helping with statistical analysis. Supercomputing time on the ARCHER UK National Supercomputing Service was provided by the "UK Consortium on Mesoscale Engineering Sciences (UKCOMES)." Funding: European Research Council: C.A.F. (679368); X.T. (883739). European Commission: C.A.F. and M.O.B. (801423); X.T. and P.R.-C. (731957). H2020-MSCA-PF grants to M.G.-G. (797621) and M.O. (842498). Fondation LeDucq: C.A.F., A.E., and M.O.B. (17CVD03). EPSRC: M.O.B. (EP/T008806/1; EP/R029598/1). Fundação para a Ciência e Tecnologia: C.A.F. (PTDC/MED-PAT/31639/2017; PTDC/BIA-CEL/32180/2017; CEECIND/04251/2017). Spanish Ministry of Science and Innovation: P.R.-C. (PID2019-110298GB-I00); X.T. (PGC2018-099645-B-I00). Generalitat de Catalunya: X.T. and P.R.-C. (2017-SGR-1602). La Caixa Foundation: X.T. and P.R.-C. (LCF/PR/HR20/52400004). Fundació la Marató de TV3: X.T. (201903-30-31-32). EMBO: L.M.F. (ALTF 2-2018)

AUTHOR CONTRIBUTIONS

Conceptualization, P.B., M.D.-C., X.T., P.R.-C., M.O.B., and C.A.F.; methodology, P.B., M.D.-C., C.G.F., G.Z., L.M.F., M.O., M.G.-G., P.R.-C., M.O.B., and C.A.F.; experimentation and data acquisition, P.B., M.D.-C., C.G.F., G.Z., A. Pena, A. Pezzarossa, D.R., Y.G., M.O., D.B., I.C.F., L.H.M., I.M., Y.C., and C.A.F.; data analysis, P.B., M.D.-C., C.G.F., L.M.F., M.G.-G., Y.G., L.H.M., X.T., P.R.-C., A.E., M.O.B., and C.A.F.; project administration, C.A.F.; writing—original draft, C.A.F.; writing—review and editing, P.B., C.G.F., L.M.F., M.O., M.G.-G., A. Pena, A. Pezzarossa, I.C.F., X.T., P.R.-C., A.E., M.O.B., and C.A.F.

DECLARATION OF INTERESTS

The authors declare no competing interests.

Received: January 19, 2022
Revised: July 15, 2022
Accepted: September 7, 2022
Published: September 28, 2022

REFERENCES

Alberding, J.P., and Secomb, T.W. (2021). Simulation of angiogenesis in three dimensions: application to cerebral cortex. PLoS Comput. Biol. *17*, e1009164.

Augustin, H.G., and Koh, G.Y. (2017). Organotypic vasculature: From descriptive heterogeneity to functional pathophysiology. Science *357*, eaal2379.

Baeyens, N., Nicoli, S., Coon, B.G., Ross, T.D., Van den Dries, K., Han, J., Lauridsen, H.M., Mejean, C.O., Eichmann, A., Thomas, J.L., et al. (2015). Vascular remodeling is governed by a VEGFR3-dependent fluid shear stress set point. eLife *4*, e04645.

Bays, J.L., and DeMali, K.A. (2017). Vinculin in cell-cell and cell-matrix adhesions. Cell. Mol. Life Sci. *74*, 2999–3009.

Bazellières, E., Conte, V., Elosegui-Artola, A., Serra-Picamal, X., Bintanel-Morcillo, M., Roca-Cusachs, P., Muñoz, J.J., Sales-Pardo, M., Guimerà, R., and Trepat, X. (2015). Control of cell-cell forces and collective cell dynamics by the intercellular adhesome. Nat. Cell Biol. *17*, 409–420.

Behnel, S., Bradshaw, R., Citro, C., Dalcin, L., Seljebotn, D.S., and Smith, K. (2011). Cython: the best of both worlds. Comput. Sci. Eng. *13*, 31–39.

Bernabeu, M.O., Jones, M.L., Nash, R.W., Pezzarossa, A., Coveney, P.V., Gerhardt, H., and Franco, C.A. (2018). PolNet: A tool to quantify network-level cell polarity and blood flow in vascular remodeling. Biophys. J. *114*, 2052–2058.

Bradski, G. (2000). The OpenCV library. Dr. Dobb's J. Softw. Tool. *25*, 120–125.

Butler, J.P., Tolić-Nørrelykke, I.M., Fabry, B., and Fredberg, J.J. (2002). Traction fields, moments, and strain energy that cells exert on their surroundings. Am. J. Physiol. Cell Physiol. *282*, C595–C605.

Cao, J., Ehling, M., März, S., Seebach, J., Tarbashevich, K., Sixta, T., Pitulescu, M.E., Werner, A.C., Flach, B., Montanez, E., et al. (2017). Polarized actin and VE-cadherin dynamics regulate junctional remodelling and cell migration during sprouting angiogenesis. Nat. Commun. *8*, 2210.

Carmeliet, P., and Jain, R.K. (2011). Principles and mechanisms of vessel normalization for cancer and other angiogenic diseases. Nat. Rev. Drug Discov. *10*, 417–427.

Cartier, A., and Hla, T. (2019). Sphingosine 1-phosphate: lipid signaling in pathology and therapy. Science *366*. eaar5551.

Carvalho, J.R., Fortunato, I.C., Fonseca, C.G., Pezzarossa, A., Barbacena, P., Dominguez-Cejudo, M.A., Vasconcelos, F.F., Santos, N.C., Carvalho, F.A., and Franco, C.A. (2019). Non-canonical Wnt signaling regulates junctional mechanocoupling during angiogenic collective cell migration. eLife *8*, e45853.

Chouinard-Pelletier, G., Jahnsen, E.D., and Jones, E.A. (2013). Increased shear stress inhibits angiogenesis in veins and not arteries during vascular development. Angiogenesis *16*, 71–83.

Chrzanowska-Wodnicka, M., and Burridge, K. (1996). Rho-stimulated contractility drives the formation of stress fibers and focal adhesions. J. Cell Biol. *133*, 1403–1415.

Claxton, S., Kostourou, V., Jadeja, S., Chambon, P., Hodivala-Dilke, K., and Fruttiger, M. (2008). Efficient, inducible Cre-recombinase activation in vascular endothelium. Genesis *46*, 74–80.

Elosegui-Artola, A., Bazellières, E., Allen, M.D., Andreu, I., Oria, R., Sunyer, R., Gomm, J.J., Marshall, J.F., Jones, J.L., Trepat, X., et al. (2014). Rigidity sensing and adaptation through regulation of integrin types. Nat. Mater. *13*, 631–637.

Figueiredo, A.M., Barbacena, P., Russo, A., Vaccaro, S., Ramalho, D., Pena, A., Lima, A.P., Ferreira, R.R., Fidalgo, M.A., El-Marjou, F., et al. (2021). Endothelial cell invasion is controlled by dactylopodia. Proc. Natl. Acad. Sci. USA *118*, e2023829118.

Fonseca, C.G., Barbacena, P., and Franco, C.A. (2020). Endothelial cells on the move: dynamics in vascular morphogenesis and disease. Vasc. Biol. *2*, H29–H43.

Franco, C.A., Blanc, J., Parlakian, A., Blanco, R., Aspalter, I.M., Kazakova, N., Diguet, N., Mylonas, E., Gao-Li, J., Vaahtokari, A., et al. (2013). SRF selectively controls tip cell invasive behavior in angiogenesis. Development *140*, 2321–2333.

Franco, C.A., Jones, M.L., Bernabeu, M.O., Geudens, I., Mathivet, T., Rosa, A., Lopes, F.M., Lima, A.P., Ragab, A., Collins, R.T., et al. (2015). Dynamic endothelial cell rearrangements drive developmental vessel regression. PLoS Biol *13*, e1002125.

Franco, C.A., Jones, M.L., Bernabeu, M.O., Vion, A.C., Barbacena, P., Fan, J., Mathivet, T., Fonseca, C.G., Ragab, A., Yamaguchi, T.P., et al. (2016). Non-canonical Wnt signalling modulates the endothelial shear stress flow sensor in vascular remodelling. eLife *5*, e07727.

Friedl, P., and Mayor, R. (2017). Tuning collective cell migration by cell-cell junction regulation. Cold Spring Harb. Perspect. Biol. *9*, a029199.

Frigo, M. (1999). A fast Fourier transform compiler. In Proceedings of the ACM SIGPLAN 1999 Conference on Programming Language Design and Implementation, *34* (Association for Computing Machinery), pp. 169–180.

Ghaffari, S., Leask, R.L., and Jones, E.A. (2015). Flow dynamics control the location of sprouting and direct elongation during developmental angiogenesis. Development *142*, 4151–4157.

Harris, C.R., Millman, K.J., van der Walt, S.J., Gommers, R., Virtanen, P., Cournapeau, D., Wieser, E., Taylor, J., Berg, S., Smith, N.J., et al. (2020). Array programming with NumPy. Nature *585*, 357–362.

Hartung, D., Aastrup Olsen, M., Xu, H., Thanh Nguyen, H., and Busch, C. (2012). Comprehensive analysis of spectral minutiae for vein pattern recognition. IET Biom *1*, 25–36.

Hasan, S.S., Tsaryk, R., Lange, M., Wisniewski, L., Moore, J.C., Lawson, N.D., Wojciechowska, K., Schnittler, H., and Siekmann, A.F. (2017). Endothelial Notch signalling limits angiogenesis via control of artery formation. Nat. Cell Biol. *19*, 928–940.

Hayer, A., Shao, L., Chung, M., Joubert, L.M., Yang, H.W., Tsai, F.C., Bisaria, A., Betzig, E., and Meyer, T. (2016). Engulfed cadherin fingers are polarized junctional structures between collectively migrating endothelial cells. Nat. Cell Biol. *18*, 1311–1323.

Hollanders, K., Van Bergen, T., Van de Velde, S., Sijnave, D., Vandewalle, E., Moons, L., and Stalmans, I. (2015). Bevacizumab revisited: its use in different mouse models of ocular pathologies. Curr. Eye Res. *40*, 611–621.

Hunter, J.D. (2007). Matplotlib: A 2D graphics environment. Comput. Sci. Eng. *9*, 90–95.

Hur, S.S., del Álamo, J.C., Park, J.S., Li, Y.S., Nguyen, H.A., Teng, D., Wang, K.C., Flores, L., Alonso-Latorre, B., Lasheras, J.C., et al. (2012). Roles of cell confluency and fluid shear in 3-dimensional intracellular forces in endothelial cells. Proc. Natl. Acad. Sci. USA *109*, 11110–11115.

Huveneers, S., Oldenburg, J., Spanjaard, E., van der Krogt, G., Grigoriev, I., Akhmanova, A., Rehmann, H., and de Rooij, J. (2012). Vinculin associates with endothelial VE-cadherin junctions to control force-dependent remodeling. J. Cell Biol. *196*, 641–652.

Jain, R.K. (2001). Normalizing tumor vasculature with anti-angiogenic therapy: a new paradigm for combination therapy. Nat. Med. *7*, 987–989.

Jalali, S., del Pozo, M.A., Chen, K., Miao, H., Li, Y., Schwartz, M.A., Shyy, J.Y., and Chien, S. (2001). Integrin-mediated mechanotransduction requires its dynamic interaction with specific extracellular matrix (ECM) ligands. Proc. Natl. Acad. Sci. USA *98*, 1042–1046.

Kapp, T.G., Rechenmacher, F., Neubauer, S., Maltsev, O.V., Cavalcanti-Adam, E.A., Zarka, R., Reuning, U., Notni, J., Wester, H.J., Mas-Moruno, C., et al. (2017). A comprehensive evaluation of the activity and selectivity profile of ligands for RGD-binding integrins. Sci. Rep. *7*, 39805.

Kechagia, J.Z., Ivaska, J., and Roca-Cusachs, P. (2019). Integrins as biomechanical sensors of the microenvironment. Nat. Rev. Mol. Cell Biol. *20*, 457–473.

Korn, C., and Augustin, H.G. (2015). Mechanisms of vessel pruning and regression. Dev. Cell *34*, 5–17.

Kwon, H.B., Wang, S., Helker, C.S., Rasouli, S.J., Maischein, H.M., Offermanns, S., Herzog, W., and Stainier, D.Y. (2016). In vivo modulation of endothelial polarization by apelin receptor signalling. Nat. Commun. *7*, 11805.

Leclech, C., Natale, C.F., and Barakat, A.I. (2020). The basement membrane as a structured surface – role in vascular health and disease. J. Cell Sci. *133*, jcs239889.

Léon, C., Eckly, A., Hechler, B., Aleil, B., Freund, M., Ravanat, C., Jourdain, M., Nonne, C., Weber, J., Tiedt, R., et al. (2007). Megakaryocyte-restricted MYH9 inactivation dramatically affects hemostasis while preserving platelet aggregation and secretion. Blood *110*, 3183–3191.

Li, S., Kim, M., Hu, Y.L., Jalali, S., Schlaepfer, D.D., Hunter, T., Chien, S., and Shyy, J.Y. (1997). Fluid shear stress activation of focal adhesion kinase. Linking to mitogen-activated protein kinases. J. Biol. Chem. *272*, 30455–30462.

Liu, Z., Tan, J.L., Cohen, D.M., Yang, M.T., Sniadecki, N.J., Ruiz, S.A., Nelson, C.M., and Chen, C.S. (2010). Mechanical tugging force regulates the size of cell-cell junctions. Proc. Natl. Acad. Sci. USA *107*, 9944–9949.

Mack, J.J., Mosqueiro, T.S., Archer, B.J., Jones, W.M., Sunshine, H., Faas, G.C., Briot, A., Aragón, R.L., Su, T., Romay, M.C., et al. (2017). NOTCH1 is a mechanosensor in adult arteries. Nat. Commun. *8*, 1620.

Martin, J.D., Seano, G., and Jain, R.K. (2019). Normalizing function of tumor vessels: progress, opportunities, and challenges. Annu. Rev. Physiol. *81*, 505–534.

McCue, S., Dajnowiec, D., Xu, F., Zhang, M., Jackson, M.R., and Langille, B.L. (2006). Shear stress regulates forward and reverse planar cell polarity of vascular endothelium in vivo and in vitro. Circ. Res. *98*, 939–946.

McKinney, W. (2010). Data structures for statistical computing in Python. In Proceedings of the 9th Python in Science Conference, pp. 56–61.

Mertz, A.F., Che, Y., Banerjee, S., Goldstein, J.M., Rosowski, K.A., Revilla, S.F., Niessen, C.M., Marchetti, M.C., Dufresne, E.R., and Horsley, V. (2013). Cadherin-based intercellular adhesions organize epithelial cell-matrix traction forces. Proc. Natl. Acad. Sci. USA *110*, 842–847.

Nehme, A., Zouein, F.A., Zayeri, Z.D., and Zibara, K. (2019). An update on the tissue renin angiotensin system and its role in physiology and pathology. J. Cardiovasc. Dev. Dis. *6*.

Park, H., Furtado, J., Poulet, M., Chung, M., Yun, S., Lee, S., Sessa, W.C., Franco, C.A., Schwartz, M.A., and Eichmann, A. (2021). Defective flow-migration coupling causes arteriovenous malformations in hereditary hemorrhagic telangiectasia. Circulation *144*, 805–822.

Park, J.Y., Yoo, S.J., Lee, E.-J., Lee, D.H., Kim, J.Y., and Lee, S.-H. (2010). Increased poly(dimethylsiloxane) stiffness improves viability and morphology of mouse fibroblast cells. BioChip J *4*, 230–236.

Pitulescu, M.E., Schmidt, I., Giaimo, B.D., Antoine, T., Berkenfeld, F., Ferrante, F., Park, H., Ehling, M., Biljes, D., Rocha, S.F., et al. (2017). Dll4 and Notch signalling couples sprouting angiogenesis and artery formation. Nat. Cell Biol. *19*, 915–927.

Potente, M., and Mäkinen, T. (2017). Vascular heterogeneity and specialization in development and disease. Nat. Rev. Mol. Cell Biol. *18*, 477–494.

Preibisch, S., Saalfeld, S., and Tomancak, P. (2009). Globally optimal stitching of tiled 3D microscopic image acquisitions. Bioinformatics *25*, 1463–1465.

Pries, A.R., Cornelissen, A.J., Sloot, A.A., Hinkeldey, M., Dreher, M.R., Höpfner, M., Dewhirst, M.W., and Secomb, T.W. (2009). Structural adaptation and heterogeneity of normal and tumor microvascular networks. PLoS Comput. Biol. *5*, e1000394.

Pries, A.R., Höpfner, M., le Noble, F., Dewhirst, M.W., and Secomb, T.W. (2010). The shunt problem: control of functional shunting in normal and tumour vasculature. Nat. Rev. Cancer *10*, 587–593.

Rothenberg, K.E., Scott, D.W., Christoforou, N., and Hoffman, B.D. (2018). Vinculin force-sensitive dynamics at focal adhesions enable effective directed cell migration. Biophys. J. *114*, 1680–1694.

Schadler, K.L., Thomas, N.J., Galie, P.A., Bhang, D.H., Roby, K.C., Addai, P., Till, J.E., Sturgeon, K., Zaslavsky, A., Chen, C.S., et al. (2016). Tumor vessel normalization after aerobic exercise enhances chemotherapeutic efficacy. Oncotarget *7*, 65429–65440.

Schneider, C.A., Rasband, W.S., and Eliceiri, K.W. (2012). NIH Image to ImageJ: 25 years of image analysis. Nat. Methods *9*, 671–675.

Scott, A., and Fruttiger, M. (2010). Oxygen-induced retinopathy: a model for vascular pathology in the retina. Eye (Lond.) *24*, 416–421.

Simons, M., Gordon, E., and Claesson-Welsh, L. (2016). Mechanisms and regulation of endothelial VEGF receptor signalling. Nat. Rev. Mol. Cell Biol. *17*, 611–625.

Song, J.W., and Munn, L.L. (2011). Fluid forces control endothelial sprouting. Proc. Natl. Acad. Sci. USA *108*, 15342–15347.

Sörensen, I., Adams, R.H., and Gossler, A. (2009). DLL1-mediated Notch activation regulates endothelial identity in mouse fetal arteries. Blood *113*, 5680–5688.

Su, T., Stanley, G., Sinha, R., D'Amato, G., Das, S., Rhee, S., Chang, A.H., Poduri, A., Raftrey, B., Dinh, T.T., et al. (2018). Single-cell analysis of early progenitor cells that build coronary arteries. Nature *559*, 356–362.

Tambe, D.T., Croutelle, U., Trepat, X., Park, C.Y., Kim, J.H., Millet, E., Butler, J.P., and Fredberg, J.J. (2013). Monolayer stress microscopy: limitations, artifacts, and accuracy of recovered intercellular stresses. PLoS One *8*, e55172.

Tambe, D.T., Hardin, C.C., Angelini, T.E., Rajendran, K., Park, C.Y., Serra-Picamal, X., Zhou, E.H., Zaman, M.H., Butler, J.P., Weitz, D.A., et al. (2011). Collective cell guidance by cooperative intercellular forces. Nat. Mater. *10*, 469–475.

Tanaka, K., Joshi, D., Timalsina, S., and Schwartz, M.A. (2021). Early Events in Endothelial Flow Sensing (Cytoskeleton).

Trepat, X., Wasserman, M.R., Angelini, T.E., Millet, E., Weitz, D.A., Butler, J.P., and Fredberg, J.J. (2009). Physical forces during collective cell migration. Nat. Phys. *5*, 426–430.

Tzima, E., del Pozo, M.A., Shattil, S.J., Chien, S., and Schwartz, M.A. (2001). Activation of integrins in endothelial cells by fluid shear stress mediates Rho-dependent cytoskeletal alignment. EMBO J *20*, 4639–4647.

Tzima, E., Irani-Tehrani, M., Kiosses, W.B., Dejana, E., Schultz, D.A., Engelhardt, B., Cao, G., DeLisser, H., and Schwartz, M.A. (2005). A mechanosensory complex that mediates the endothelial cell response to fluid shear stress. Nature *437*, 426–431.

Tzima, E., Kiosses, W.B., del Pozo, M.A., and Schwartz, M.A. (2003). Localized cdc42 activation, detected using a novel assay, mediates microtubule organizing center positioning in endothelial cells in response to fluid shear stress. J. Biol. Chem. *278*, 31020–31023.

van der Walt, S., Schönberger, J.L., Nunez-Iglesias, J., Boulogne, F., Warner, J.D., Yager, N., Gouillart, E., and Yu, T.; Scikit-Image Contributors (2014). scikit-image: image processing in Python. PeerJ *2*, e453.

Vasioukhin, V., Bauer, C., Degenstein, L., Wise, B., and Fuchs, E. (2001). Hyperproliferation and defects in epithelial polarity upon conditional ablation of alpha-catenin in skin. Cell *104*, 605–617.

Vion, A.C., Perovic, T., Petit, C., Hollfinger, I., Bartels-Klein, E., Frampton, E., Gordon, E., Claesson-Welsh, L., and Gerhardt, H. (2020). Endothelial cell orientation and polarity are controlled by shear stress and VEGF Through distinct signaling pathways. Front. Physiol. *11*, 623769.

Virtanen, P., Gommers, R., Oliphant, T.E., Haberland, M., Reddy, T., Cournapeau, D., Burovski, E., Peterson, P., Weckesser, W., Bright, J., et al. (2020). SciPy 1.0: fundamental algorithms for scientific computing in Python. Nat. Methods *17*, 261–272.

Vitorino, P., and Meyer, T. (2008). Modular control of endothelial sheet migration. Genes Dev *22*, 3268–3281.

Wood, J.A., Liliensiek, S.J., Russell, P., Nealey, P.F., and Murphy, C.J. (2010). Biophysical cueing and vascular endothelial cell behavior. Materials *3*, 1620–1639.

Xanthis, I., Souilhol, C., Serbanovic-Canic, J., Roddie, H., Kalli, A.C., Fragiadaki, M., Wong, R., Shah, D.R., Askari, J.A., Canham, L., et al. (2019). β1 integrin is a sensor of blood flow direction. J. Cell Sci. *132*, jcs229542.

STAR★METHODS

KEY RESOURCES TABLE

REAGENT or RESOURCE	SOURCE	IDENTIFIER
Antibodies		
Rat monoclonal anti-ICAM2	BD Biosciences	Cat# 553326; RRID: AB_394784
Rabbit polyclonal anti-pPaxilin-Y118	Cell Signaling	Cat# 2541S; RRID: AB_2174466
Rabbit monoclonal anti-ERG	Abcam	Cat# ab92513; RRID: AB_2630401
Goat polyclonal anti-rat Alexa 555	Thermo Scientific	Cat# A21434; RRID: AB_2535855
Donkey polyclonal anti-rabbit Alexa 488	Thermo Scientific	Cat# A21206; RRID: AB_2535792
Goat polyclonal anti-CD31	R&D	Cat# AF3628; RRID: AB_2161028
Donkey polyclonal anti-rabbit Fab2 fragments	Jackson ImmunoResearch	Cat# 711-006-152; RRID: AB_2340586
Rabbit polyclonal anti-GOLPH4	Abcam	Cat# ab28049; RRID: AB_732692
Goat polyclonal anti-Klf4	R&D	Cat# AF3158; RRID: AB_2130245
Goat polyclonal anti-rabbit Alexa 647	Thermo Scientific	Cat# A31573; RRID: AB_2536183
Rat monoclonal anti-Cdh5	BD biosciences	Cat# 555289; RRID: AB_395707
Rabbit polyclonal anti-AKT	Cell Signaling	Cat# 9272; RRID: AB_329827
Goat polyclonal anti-VEcadherin	R&D	Cat# AF938; RRID: AB_355726
Mouse monoclonal anti-Vinculin	Sigma-Aldrich	Cat# V9264; RRID: AB_10603627
Rabbit monoclonal anti-ITGA5	Abcam	Cat# ab150361; RRID: AB_2631309
Rat monoclonal anti-activated ITGB1	BD Pharmingen	Cat# 553715; RRID: AB_395001
Rabbit polyclonal anti-pPaxillin	Cell Signaling	Cat# 2541S; RRID: AB_2174466
Rabbit monoclonal anti-FAK	Cell Signaling	Cat# 71433; RRID: AB_2799801
Rabbit monoclonal anti-pNF-kB p65 S536	Cell Signaling	Cat# 3033; RRID: AB_331284
Donkey polyclonal anti-goat Alexa 647	Thermo Scientific	Cat# A21447; RRID: AB_2535864
Donkey polyclonal anti-mouse Alexa 488	Thermo Scientific	Cat# A21202; RRID: AB_141607
Donkey polyclonal anti-rabbit Alexa 568	Thermo Scientific	Cat# A10042; RRID: AB_2534017
Rabbit monoclonal anti-Talin	Cell Signaling	Cat# 4021; RRID: AB_2204018
Mouse monoclonal anti-ßactin	Sigma	Cat# A5441; RRID: AB_476744
Rabbit polyclonal anti-pVinculin Y100	Thermo Scientific	Cat# 44-1074G; RRID: AB_2533566
Mouse monoclonal anti-VE-cadherin	Santa Cruz Biotechnology	Cat# sc-9989; RRID: AB_2077957
Rabbit polyclonal anti-αCatenin	Sigma-Aldrich	Cat# C2081; RRID: AB_476830
Rabbit monoclonal anti-pAKT S473	Cell Signaling	Cat# 4060; RRID: AB_2315049
Mouse monoclonal anti-NFkB p65	Cell Signaling	Cat# 6956; RRID: AB_10828935
Rabbit monoclonal anti-pFAK Y397	Cell Signaling	Cat# 8556; RRID: AB_10891442
Rabbit polyclonal anti-vinculin	Sigma-Aldrich	Cat# V4139; RRID: AB_262053
Chemicals, peptides, and recombinant proteins		
Angiotensin-II	Sigma-Aldrich	Cat#A9525
Captopril	Sigma-Aldrich	Cat#C4042
Recombinant VEGFA	R&D Systems	Cat#493-VE-050
sFLT1	R&D Systems	Cat#471-F1-100
Paraformaldehyde	Sigma-Aldrich	Cat#4412244
Y-27632	Merck Millipore	Cat#688001
4-hydroxytamoxifen	Sigma-Aldrich	Cat#H6278
DharmaFECT 1 reagent	Dharmacon, GE Healthcare	Cat#T-2001-02
(−)-Blebbistatin	Sigma-Aldrich	Cat#B0560
RGDS	Tocris	Cat#3498
Puromycin	Sigma-Aldrich	Cat#P8333

(*Continued on next page*)

Continued

REAGENT or RESOURCE	SOURCE	IDENTIFIER
Triptolide	Sigma-Aldrich	Cat#T3652
Power SYBR Green PCR Master Mix	Applied Biosystems	Cat#4368702
Triton X-100	Sigma-Aldrich	Cat#T8787
Vectashield mounting medium	Vector Laboratories	Cat#H-1000
TrypLE™ Express Enzyme (1X)	Alfagene	Cat#12605028
Gelatin solution	Sigma-Aldrich	Cat#G1393
Penicillin/Streptomycin	Gibco	Cat#15140122
Phosphatase and proteinase inhibitors cocktail	Thermo Scientific	Cat#10085973
4x Laemmli Sample Buffer	Bio-rad	Cat#161-0747
DTT	Sigma-Aldrich	Cat#D0632
Sulfo-SANPAH	Thermo Scientific	Cat#22589
APTS	Sigma-Aldrich	Cat#A3648
FluoSpheresCarboxylate-Modified Microspheres beads	Invitrogen	Cat#F8810
$Na_2BO_4O_7$	Sigma-Aldrich	Cat#221732
H_3BO_3	Sigma-Aldrich	Cat#B1934
Critical commercial assays		
RNeasy Micro Kit	Qiagen	Cat#50974004
GeneJet RNA Purification Kit	Thermo Scientific	Cat#K0702
Duolink In Situ Red Mouse/Rabbit Starter Kit	Sigma-Aldrich	Cat#DUO92101-1KT
BCA protein assay kit	Thermo Scientific	Cat#23227
ECL™ Western Blotting Detection Reagent 24	GE Healthcare	Cat#RPN2209
Superscript IV First-Strand Synthesis System	Invitrogen	Cat#18091050
Dow Corning 184 Sil. Elastomer Kit	Ellsworth Adhesives Ibérica SL	Cat#0002-04-000002
Experimental models: Cell lines		
HUVEC Passage 1-5	Lonza	Cat#C2519A
HEK293T Passage 20-25	ATCC	Cat#CRL3216
Experimental models: Organisms/strains		
Mouse: Myh9 floxed	Léon et al., 2007	N/A
Mouse: Ctnna1 floxed	Vasioukhin et al., 2001	N/A
Mouse: PdgfbiCreERT2	Claxton et al., 2008	N/A
Mouse: Cdh5CreERT2	Sörensen et al., 2009	N/A
Mouse: C57BL/6	Instituto de Mecicina Molecular (born in house)	N/A
Oligonucleotides		
Human siRNAs against CTNNA1	Horizon Discovery	Cat#J-010505-06
Human siRNAs against CHD5	Horizon Discovery	Cat#J-003641-07
Human siRNAs against KDR	Horizon Discovery	Cat#J-003148-10
Human siRNAs against PECAM1	Horizon Discovery	Cat#J-017029-08
See Table S1 for additional information on oligonucleotides used for qPCR	N/A	N/A
Recombinant DNA		
pRRL-VinculinTS	Addgene	Plasmid #111830
ΔR8.2	Addgene	Plasmid #12263
VSVG	Addgene	Plasmid #45494

(*Continued on next page*)

Continued

REAGENT or RESOURCE	SOURCE	IDENTIFIER
Software and algorithms		
ImageJ	Schneider et al., 2012	https://imagej.nih.gov/ij/
MATLAB	The MathWorks, Inc	https://matlab.mathworks.com/
PolNet	Bernabeu et al., 2018	http://ltc.amu.edu.pl/polnet/index.php
GraphPad Prism 7	GraphPad	https://www.graphpad.com/
Photoshop	Adobe	https://www.adobe.com/pt/products/photoshop.html
SciPy	Virtanen et al., 2020	https://scipy.org/download/
Matplotlib	Hunter, 2007	https://matplotlib.org/stable/users/installing/index.html
Opencv	Bradski, 2000	https://opencv.org/releases/
pyFFTW	Frigo, 1999	https://pypi.org/project/pyFFTW/
Python 3	Harris et al., 2020	https://www.python.org/downloads/
NumPy	Harris et al., 2020	https://numpy.org/install/
Scikit-image	van der Walt et al., 2014	https://scikit-image.org/docs/stable/install.html
Cython	Behnel et al., 2011	https://pypi.org/project/Cython/
Pandas	McKinney, 2010	https://pandas.pydata.org/docs/getting_started/install.html
Imaris 9.8	Oxford Instruments	https://imaris.oxinst.com/
Vessel Morphometrics	This study	https://doi.org/10.5281/zenodo.7036288
Other		
Cytocentric® O2 Controller	BioSpherix, USA	Cat#ProOx 110
EGM-2 Bulletkit	Lonza	Cat#CC-3162
Leibovitz L15 media	Life technologies, LTI	Cat#21083-027
iBIDI μ-Slide I 0.4 Luer	iBIDI	Cat#80176
Minipuls3 peristaltic pump	Gilson	Cat#GM3P4
4-15% Mini-PROTEANTGX Ge	Bio-Rad	Cat#456-1084
DAPI	Life Technologies	Cat#D1306; RRID: AB_2629482

RESOURCE AVAILABILITY

Lead contact

Further information and requests for resources and reagents should be directed to and will be fulfilled by the lead contact, Cláudio A. Franco (cfranco@medicina.ulisboa.pt).

Materials availability

This study did not generate new unique reagents.

Data and code availability

- All data reported in this paper, including microscopy data or MSM data required to reanalyze the data reported in this paper will be shared by the lead contact upon request.
- Original code related to Plexus Morphometrics has been deposited at Zenodo and is publicly available as of the date of publication. DOI is listed in the key resources table. Matlab scripts used to analyse data in this paper is available in the supplemental information file.
- Any additional information required to reanalyze the data reported in this paper is available from the lead contact upon request.

EXPERIMENTAL MODEL AND SUBJECT DETAILS

Mice

In this study, we used the following mouse strains: Myh9 floxed (Léon et al., 2007); Ctnna1 floxed (Vasioukhin et al., 2001); PdgfbiCreERT2 (Claxton et al., 2008); Cdh5CreERT2 (Sörensen et al., 2009); and WT C57BL/6. C57BL/6 pups were used for

modulation of flow, VEGF availability or drug treatment. No distinction of sex of animals was considered in this study. Mice were maintained and breed at the Instituto de Medicina Molecular João Lobo Antunes (IMM-JLA) under standard husbandry conditions and under Portuguese regulations. For instance, mice were housed four to five per cage, and allowed free access to water and food. Breedings were performed in duos or trios, and pups were kept all time with mothers during treatments, with the exception of OIR experiments, where pups were kept only the mother.

Ethics statement

Animal experimentation was carried out in compliance with EU Directive 86/609/EEC and Recommendation 2007/526/EC regarding the protection of animals used for experimental and other scientific purposes. Animal procedures were performed under supervision by the IMM-JLA Animal Ethics Committee (ORBEA), under the project licenses AWB_2015_10_CF_Polaridade and AWB_2021_02_CF_Vascular, and approved by the Portuguese Animal Ethics Committee regulatory body (DGAV), project licenses 0421/000/000/2016 and 0421/000/000/2021.

Culture of HUVECs

Human umbilical vein endothelial cells – HUVECs (Lonza, C2519A) – were cultured following the manufacturer's guidelines, in filter-cap T75 flasks Nunclon Δ surface treatment (VWR international, LLC) with complete medium EGM-2 Bulletkit (Lonza, CC-3162) at 37°C and 5% CO_2 to ensure stable environment for optimal cell growth. All the experiments were conducted with HUVECs between passages 1 and 5. When passaging HUVECs for experiments, cells were washed twice in sterile PBS (137mM NaCl, 2.7mM KCl, 4.3mM Na_2HPO_4, 1.47mM KH_2PO_4, pH7.4) and then incubated for 5min in TrypLE™ Express Enzyme (1X) (Alfagene, 12605028) at 37°C, 5% CO_2. When 95% of the cells detached, complete medium was added to each flask to inhibit the activity of the TrypLE™ Express Enzyme and the cell suspension was transferred into a falcon tube. Cells were then centrifuged at 700rpm for 5min at RT and the pellet re-suspended in fresh complete medium. HUVECs were then seeded at the desired concentration, depending on the experiments.

METHOD DETAILS

In vivo mouse treatments

For increasing blood flow, angiotensin II (Sigma-Aldrich, A9525) was injected intraperitoneally (IP) 10μL/g (10 mg/mL stock solution) daily at postnatal day 3 (P3), P4 and P5 and pups were collected at P6. On the opposite, to reduce blood flow, captopril (Sigma-Aldrich, C4042) was injected IP 15μL/g (3.3mg/mL stock solution) daily at P3, P4 and P5 and pups were collected at P6. In both experiments, control mice were injected using PBS alone. For intraocular administration of reagents, P4-P5 pups were anesthetized and intravitreal injections were performed under a stereomicroscope using a 10μl Hamilton syringe equipped with a 33-gauge needle. Approximately 0.5μl of sterile solution or PBS was injected per eye, while the contralateral eye remained uninjected. The following substances were used: recombinant VEGFA (493-VE-050; R&D Systems, 3μg/μl) or recombinant VEGFR1/Flt-1 Fc chimera protein (sFLT1; 471-F1-100; R&D Systems, 1μg/μl). Mice were sacrificed 36h later. The eyes were removed, fixed in 2% paraformaldehyde (PFA, Sigma-Aldrich, 4412244) in PBS at 4°C for 5h, rinsed in PBS and processed for IHC. In the case of Y-27632 treatment, Y-27632 (Merck Millipore, 688001) was injected IP (10mg/kg) at P5 and pups were sacrificed at P6.

In gene deletion experiments, 4-hydroxytamoxifen (Sigma-Aldrich, H6278) was injected IP (20 μg/g) at P1 and P3 for Myh9 floxed mice and at P4 for Ctnna1 floxed, and eyes were collected at P6. As controls, Cre-negative littermates were used in all experiments. Both males and females were used, without distinction.

In OIR experiments, P8 pups and their nursing mothers were housed into an air-tight chamber and exposed to 75% oxygen level in air maintained by a ProOx 110 oxygen controller (BioSpherix, USA). They were returned to room air at P11, also named D0 for day 0 after return to normoxia. In OIR animals, Captopril (C4042, Sigma Aldrich, Germany) (50 μg/g), Angiotensin II (A9525, Sigma Aldrich, Germany) (100 μg/g) or vehicle (PBS) was injected IP at D4, D5, and D6 and pups were sacrificed at D7. Eyes were collected and fixed with 2% PFA in PBS overnight at 4°C.

Viral production and transduction

Replication-incompetent lentiviruses were produced by transient transfection of HEK293T with lentiviral expression vector co-transfected with the viral packaging vector ΔR8.2 and the viral envelope vector VSVG. Medium was replaced with fresh culture medium 6-8h post transfection. 48h after medium replacement, lentiviral particles were concentrated from supernatant by ultracentrifugation at 112.500g for 1h30 and re-suspended in 0.1% BSA PBS. Seeded HUVECs were transduced with varying concentrations of a lentiviral plasmid containing pRRL-VinculinTS (Rothenberg et al., 2018). 24h after viral transduction the culture medium was replaced by fresh complete medium and cells were kept under culture conditions up until 72h post-transduction and then processed for imaging.

Immunofluorescence on mouse retinas

Retinas were stained as previously described (Franco et al., 2013). Briefly, retinas were incubated for 2h, at RT in Claudio's Blocking Buffer (CBB). For polarity experiments, retinas were incubated with anti-ICAM2 (1:100, BD Biosciences 553326) and anti-ERG (1:200, Abcam ab92513) primary antibodies in 1:1 PBS and CBB mixture at 4°C o/n. On the next day, retinas were washed 3 times (30min each) with PBST (PBS with 0.1% Triton X-100, Sigma-Aldrich, T8787) and further incubated with secondary antibodies anti-rat Alexa

555 (Thermo Fisher Scientific, A21434) and anti-rabbit Alexa 488 (Thermo Fisher Scientific, A21206) in 1:1 PBS and CBB mixture o/n at 4°C. The day after, retinas were washed three times (30min each) with PBST and incubated with Fab_2 fragments (Donkey anti-rabbit, Jackson ImmunoResearch, 711-006-152) for 2h at RT with gentle shaking. Afterwards retinas were fixed with 4% paraformaldehyde (PFA) at RT for 15min and washed three times (15min each) with PBST, followed by 1h incubation with CBB at RT. Next, retinas were incubated with anti-GOLPH4 primary antibody (1:400, Abcam, ab28049) in 1:1 PBS and CBB mixture at 4°C o/n. The day after, retinas were washed three times (30min each) with PBST and incubated with anti-rabbit Alexa 647 (Thermo Fisher Scientific, A31573) secondary antibody in 1:1 PBS and CBB o/n at 4°C. Then, retinas were washed three times (30min each) with PBST and flat-mounted on glass slides using Vectashield mounting medium (Vector Laboratories, H-1000). Additional antibodies were used: anti-CD31 (R&D, AF3628, 1:200), anti-pPaxilin-Y118 (Cell Signaling, 2541S, 1:100), anti-Cdh5 (BD biosciences, 555289, 1:25), anti-Klf4 (R&D, AF3158, 1:50). Images were acquired by tile-scans with multiple Z-positions using a Zeiss Cell Observer SD (Carl Zeiss) equipped with Zen software and with a Plan-Apochromat 40x NA 1.40 oil or Plan-Apochromat 63x NA 1.40 objectives.

siRNA transfection

In order to silence the expression of genes of interest, a set of ON-TARGET human siRNAs against CTNNA1 (Dharmacon, GE Healthcare, J-010505-06), CDH5 (Dharmacon, GE Healthcare, J-003641-07) or untargeting control were used. Briefly, HUVECs were seeded the day before the transfection to reach 60-70% confluence and were then transfected with 25nM of siRNA using the DharmaFECT 1 reagent (Dharmacon, GE Healthcare) following the Dharmacon siRNA Transfection Protocol. 24h after transfection the culture medium was replaced by fresh complete medium and cells were kept under culture conditions up until 72h post-transfection and then processed for further experiments.

Flow microfluidic assays

For the flow microfluidics assay, HUVECs were plated at a concentration of $3x10^6$ cells/mL onto iBIDI μ-Slide I $^{0.4}$ Luer (iBIDI, 80176), previously coated with 0.2% gelatin solution in H_2O (Sigma-Aldrich, G1393), 4h prior flow application. When transfected cells were used, they were plated 68h after transfection. Flow culture medium consisted of Leibovitz L15 media (Life technologies, LTI 21083-027) supplemented with EGM-2 SingleQuots™ (Lonza, CC-4176) and 1% penicillin/streptomycin (Gibco, #15140122). After 4h of attachment, HUVECs were subjected to flow at different ranges, depending on the experiment, for 4 hours or the appropriate amount of time. The iBIDI slides were connected to a peristaltic pump (Gilson Minipuls3) that ensures a continuous laminar flow during the experiments.

For the flow and scratch wound-assay set of experiments, HUVECs were plated onto microscopy glass slides (Thermo Scientific, 76x26mm) coated with 0.2% gelatin solution in H_2O (Sigma-Aldrich, G1393) at $3x10^6$ cells/mL. When HUVECs reached confluence, a wound was created by scratching the surface of the microscopy glass slide with a 200μL pipette tip. The culture medium was then replaced by fresh complete medium and HUVECs were allowed to migrate under flow, using sticky-Slide I $^{0.4}$ Luer (iBIDI, 80178) for 5 hours.

When assessing the effects of VEGFA and KDR in polarity assays, Leibovitz L15 media supplemented with 50ng/mL hVEGFA (Prepotech) was used instead of EGM-2 SingleQuots.

Drugs assays

For the experiments with inhibitors, HUVECs were seeded at $3x10^6$ cells/mL in iBIDI μ-Slide I $^{0.4}$ Luer (iBIDI, 80176), previously coated with 0.2% gelatin solution in H_2O (Sigma-Aldrich, G1393), 4h prior flow application. Inhibitors were added to the media 1h before the flow microfluidic assay at specific concentrations. When indicated, cells were treated with (−)-Blebbistatin (20μM, Sigma-Aldrich, B0560), Y-27632 (5μM, Merck Millipore, 688001), RGDS (20μM, Tocris, 3498), Puromycin (200μg/ml, Sigma-Aldrich, P8333) and Triptolide (2μM, Sigma-Aldrich, T3652).

Immunofluorescence of cultured HUVECs

For immunofluorescence of *in vitro* cultured HUVECs, cells were fixed in 1% PFA *Sigma-Aldrich, 4412244) in PBS for 30min at RT. Fixed HUVECs were blocked and permeabilized with blocking solution containing 3% BSA, 0.1% Triton X100 in PBS for 30min at RT. Then cells were incubated for 2h at RT with the appropriate primary antibodies diluted in the blocking solution (anti-VE-cadherin, R&D - AF938, 1:50; anti-GOLPH4, Abcam - ab28049, 1:400; anti-Vinculin, Sigma-Aldrich - V9264, 1:400; anti-ITGA5, Abcam - ab150361, 1:100; anti-pPaxillin, Cell Signaling - 2541S, 1:100; anti-activated ITGB1 BD Pharmingen - 553715, 1:100) and washed 3 x 15min with PBST. Afterwards, cells were incubated in blocking solution containing the secondary fluorophore conjugated antibodies for 1h at RT in the dark (Donkey anti-goat Alexa 647, Thermo Fisher Scientific - A21447, 1:400; Donkey anti-mouse Alexa 488, Thermo Fisher Scientific - A21202, 1:400; Donkey anti-rabbit Alexa 568, Thermo Fisher Scientific - A10042, 1:400), followed again by 3 washes of 15min in PBST. Finally, HUVECs were incubated with 1x DAPI (Molecular Probes by Life Technologies, D1306) diluted in PBS for 5min in the dark. For morphological or colocalization analysis, high-resolution Z-stack images at multiple positions were acquired on a confocal Laser Point-Scanning Microscope 880 (Zeiss) equipped with the Zen black software with a Plan Apochromat 63x NA 1.40 oil DIC M27 objective. For polarization analysis, images at multiple positions were acquired on Zeiss Axiovert 200M equipped with an EC Plan-NeoFluar 40x NA 0.75.

Protein extraction and western blotting

Protein extraction was performed from HUVECs lysed in 120μL of RIPA buffer supplemented with phosphatase and proteinase inhibitors cocktail (1:100, Fischer Scientific, #10085973). Adherent cells were then detached from the plate with a cell scrapper and the cell lysates were transferred into an ice cold eppendorf tube and centrifuged at maximum speed for 10min at 4°C. Protein concentration was quantified using the BCA protein assay kit (Pierce™, Thermo Fisher Scientific, 23227) following the manufacturer's guidelines. The Multimode microplate reader, Infinite M200 (TECAN), was used for spectrophotometric measurement of protein with the i-control™ software. For Western Blotting, protein samples were normalized up to 25μL and combined with a mixture of 4x Laemmli Sample Buffer (Bio-rad Laboratories, #161-0747) with 450mM DTT (SigmaAldrich, D0632) and incubated at 95°C for 5min. Protein samples were loaded and separated on a 4-15% Mini-PROTEANTGX Gel (BioRad, #456-1084) along with 5μL of protein ladder (GE Healthcare, RPN800E). After transfer, blotted membranes were incubated in Ponceau Red to assess transfer quality, and then washed in TBST (50mM Tris/HCl, 150mM NaCl, 0.1% Tween-20, pH7.5). Afterwards, membranes were incubated in blocking solution containing 3% BSA in TBST for 1h at RT, followed by an o/n incubation at 4°C with the primary antibodies diluted in the same blocking buffer, anti-pPaxillin Y118 (Cell Signalling - 2541S, 1:1000), anti-ßactin (Sigma, A5441, 1:5000), anti-Vinculin (Sigma-Aldrich, V9264, 1:1000), anti-pVinculin Y100 (Thermo Fisher Scientific, 44-1074G, 1:1000), anti-VE-cadherin (Santa Cruz Biotechnology, sc-9989, 1:1000), anti-αCatenin (Sigma-Aldrich, C2081, 1:1000), anti-Talin(Cell Signaling, 4021, 1:1000), anti-AKT (Cell Signaling, 9272, 1:1000), anti-pAKT S473 (Cell Signaling, 4060, 1:1000), anti-FAK (Cell Signaling, 71433, 1:1000), anti-pFAK Y397 (Cell Signaling, 8556, 1:1000), anti-NF-kB p65 (Cell Signaling, 6956, 1:1000) and anti-pNF-kB p65 S536 (Cell Signaling, 3033, 1:1000). On the following day membranes were washed 3 times in TBST and incubated with secondary horseradish peroxidase (HRP)-conjugated antibodies for 1h at RT. Before revelation, membranes were washed again 3 times in TBST for 5min and then incubated in ECL™ Western Blotting Detection Reagent 24 (GE Healthcare, RPN2209) following the manufacturer's protocol. Protein bands were visualized in Amersham 680 (Cytiva) and relative protein quantities were measured using FIJI software (Schneider et al., 2012).

RNA extraction and cDNA synthesis

RNA extraction from HUVECs. HUVECs RNA extraction using the RNeasy Micro Kit (Qiagen) and the GeneJet RNA Purification Kit (Thermo Scientific) as described by the manufacturer's protocol. RNA concentration was quantified using NanoDrop 1000 (Thermo Scientific) and adjusted equally, followed by DNase I digestion (Thermo Scientific) and cDNA synthesis (Superscript IV First-Strand Synthesis System, Invitrogen). In some cases, a spike-in RNA control was added to the mixture in order to control for gene expression during the real-time quantitative PCR (RT-qPCR). cDNA samples were then diluted in RNAse/DNAse-free water for the subsequent RT-qPCR reactions.

RNA extraction from mouse retinas. Pair of retinas from the same animal were dissected in ice-cold fresh PBS and immediately snap frozen in liquid nitrogen. Retinas were lysed in RLT buffer from the RNeasy Micro Kit (Qiagen) vortexed vigorously and further homogenized using 30g syringe needles. Lysates were centrifuged to clear from precipitates, and supernatant was used for RNA extraction as described by the manufacturer's protocol, including in column DNase I treatment. RNA concentration was quantified using NanoDrop 1000 (Thermo Scientific) and adjusted equally cDNA synthesis (Superscript IV First-Strand Synthesis System, Invitrogen). cDNA samples were then diluted in RNAse/DNAse-free water for the subsequent real-time quantitative PCR (RT-qPCR) reactions.

RT-qPCR

RT-qPCR was performed using a 7500 Fast Real-Time PCR System (Applied Biosystems) with Power SYBR Green PCR Master Mix (Applied Biosystems) following the standard program of the system previously mentioned. For each reaction, 5μL of cDNA was combined with 10μL of Power SYBR Green PCR Master Mix, 4.5μL of RNAse/DNAse free water and 0.5μL of 4μM primers pool (Forward+Reverse) in a MicroAmp Fast Optical 96-well Reaction Plate (Applied Biosystems).

The expression levels of each sample duplicate were then normalized to GAPDH or spike-in RNA and the $2^{-\Delta\Delta T}$ method was used to calculate relative alterations in gene expression. Primers used in this paper are provided as Table S1.

PDMS gels

PDMS (Polydimethylsiloxane) was produced with different stiffness. Briefly, Silicone Elastomer (Sylgard 184 Silicone Elastomer, Dow 101697) was mixed with curing agent (Sylgard 184 Silicone Elastomer, Dow 101697) at three different ratios (by weight): 5:1; 10:1 and 20:1, corresponding to a Young's elastic modulus of 1000kPa; 580kPa and 280kPa, respectively, followed by degassing in a vacuum chamber for 30min at RT and cured by heating in an oven at 75°C for 2h, as previously reported (Park et al., 2010). After polymerization, PDMS gels were demolded and sterilized. Afterward, gels were coated with 0.2% gelatin solution in H_2O for 30min at 37°C and HUVECs seeded as described before for flow experiments.

Soft-PDMS gels with different stiffnesses were produced to measure the focal adhesion length in ECs under shear stress. Briefly, solution A and B (DOWSIL™ CY 52-276 A&B, Dow) were mixed in a 1:1 or 5:6 (w/w) ratio corresponding to a bulk elastic modulus of 3kPa and 18.6 kPa respectively, followed by degassing in a vacuum chamber for 30min on ice. Afterwards, 2ml of soft-PDMS were added to glass slides and spun for 90s, 24V in a handmade spin-coater. Finally, slides with soft-PDMS were cured by heating in an oven at 65°C o/n.

To promote better cell adhesion, soft-PDMS gels were incubated with 0.2mg/ml of Sulfo-SANPAH (sulfosuccinimidyl 6-(4'-azido-2'-nitrophenylamino) hexanoate, Thermo Scientific) twice during 5 min under UV lamp (approximately 365nm) and washed twice with

50mM of HEPES (Gibco). Finally, soft-PDMS gels were coated with 0.2% gelatin solution in H_2O for 30min at 37°C and HUVECs seeded 4h prior flow experiments as described previously.

Traction force microscopy and monolayer stress microscopy

For the TFM experiments, soft-PDMS gels (1:1 ratio) were produced as described previously (Park et al., 2010). To coat with fluorescent beads, 5% APTES (SIGMA, A3648) was used to silanise the soft-PDMS and the gels were washed three times with EtOH absolute. The glass slides with the soft-PDMS were then dried in an oven at 60°C for 10min. FluoSpheresCarboxylate-Modified Microspheres beads (Invitrogen, F8810) were diluted (1:50) in a boric solution ($Na_2BO_4O_7$, SIGMA 221732 and H_3BO_3, SIGMA B1934), filtered with a 0.45μm filter and sonicated for 10min. Afterwards, fluorescent beads were added to the soft-PDMS gels and incubated for 5min at RT. Gels were then dried in an oven at 60°C. Then, gels were incubated with 0.2mg/ml of Sulfo-SANPAH [sulfosuccinimidyl 6-(4'-azido-2'-nitrophenylamino) hexanoate, Thermo Scientific] twice during 5 min under UV lamp (approximately 365nm) and washed twice with 50mM of HEPES (Gibco). Finally, soft-PDMS gels were coated with 0.2% gelatin solution in H_2O for 30min at 37°C and HUVECs seeded 4h prior flow experiments.

Traction force measurements were performed as described previously (Butler et al., 2002). For each condition, fluorescent images of cell monolayers and nanobeads placed on the surface of the gels were imaged in Leica SP8 multi-photon microscope using the Insight DS+ Dual pulsed laser at 920nm and using a Leica 20x objective (NA 0.95) using tile scans of 4x4 fields-of-view. At the end of the measurements, cells were detached from the gel with 10x trypsin/EDTA (Gibco) and an image of bead position in the relaxed state of the gel was acquired. Individual tiles of each field of view were stitched by using FIJI (Schneider et al., 2012) and the Grid/Collection stitching plugin (Preibisch et al., 2009). 2D images of the deformed substrate were compared to the relaxed state with a custom-made PIV software in Matlab (MathWorks) to obtain the 2D deformation of the top layer of the gel. Fineite-thickness Fourier-transform traction force microscopy was then used to calculate the traction forces exerted by the cells (Elosegui-Artola et al., 2014; Trepat et al., 2009). The average forces per unit area exerted by each monolayer were then calculated. To calculate the minimum detectable force levels, we followed the same procedure in cell-free gel areas, and calculated the resulting forces.

Monolayer Stress Microscopy (Tambe et al., 2011, 2013) was used to calculate the monolayer tension from the traction fields. It was implemented, as a custom-made software, in Python 3 using NumPy (Harris et al., 2020), SciPy (Virtanen et al., 2020), Matplotlib (Hunter, 2007), scikit-image (van der Walt et al., 2014), pandas (McKinney, 2010), pyFFTW (Frigo, 1999), opencv (Bradski, 2000) and cython (Behnel et al., 2011).

Proximity ligation assay

After flow microfluidic experiments, HUVECs were processed for PLA using the Duolink In Situ Red Mouse/Rabbit Starter Kit (Sigma-Aldrich, DUO92101-1KT) as described by the manufacturer's protocol. To probe interactions between VINCULIN and VE-cadherin, cells were incubated with an anti-vinculin antibody raised in rabbit (Sigma-Aldrich, V4139) and an anti-VE-cadherin antibody raised in mouse (Santa Cruz Biotechnologies, sc-9989). In parallel, cells were also incubated with an anti-VE-cadherin antibody raised in goat (R&D Systems, AF938) and subsequently with an anti-goat Alexa 647 secondary antibody (Thermo Fisher Scientific, A21447) to label adherens junctions. To probe interactions between VINCULIN and ITGA5, cells were incubated with an anti-vinculin antibody raised in mouse (Sigma-Aldrich, V9264) and an anti-ITGA5 antibody raised in rabbit (Abcam, ab150361).

To quantify colocalization of PLA signal at adherens junctions, high-resolution Z-stack images at multiple positions were acquired on a confocal Laser Point-Scanning Microscope 880 (Zeiss) equipped with the Zen black software with a Plan Apochromat 63x NA 1.40 oil DIC M27 objective. Briefly, PLA dots were quantified using ImageJ' particle analysis tool and the data normalized by the number of cells.

QUANTIFICATION AND STATISTICAL ANALYSIS

Tension sensor FRET measurements

Cells infected with the viral plasmid pRRL-VinculinTS (Rothenberg et al., 2018) were used for these experiments. FRET images were obtained using a confocal Laser Point-Scanning Microscope 880 (Zeiss) equipped with a Plan-Apochromat 63x, NA 1.40, oil immersion, DIC M27 objective and an argon laser featuring 405, 458 and 514nm laser lines. For FRET experiments, an MBS 458/514 beam splitter was used in combination with the following filters: mTFP1 GaAsP, band-pass 461–520; Venus/FRET, band-pass 525–575. Acceptor photobleaching experiments were analyzed using a custom written MATLAB script. A Gaussian filter with standard deviation of 0.75 was applied to the images before analysis. The intensity in the region of interest was measured before and after bleaching. FRET efficiency was calculated as $EF = \frac{Ipost - Ipre}{Ipost}$, where Ipost and Ipre are the intensity of the donor channel after and before bleaching respectively.

Quantification of Focal Adhesions and Colocalization Analysis

To quantify number and size of focal adhesions, co-immunostainings for vinculin and ITGA5 together with VE-cadherin were performed to identify structures that shared vinculin and ITGA5 staining. The number of these structures were then quantified per cell, defined by the VE-cadherin contour. To quantify size of focal adhesions, vinculin-ITGA5 structures were selected and the vinculin staining only was then used to perform measurements.

For colocalization analyses, high-resolution Z-stack confocal images of HUVECs stained for different proteins (VE-Cadherin, Vinculin and ITGA5) were imported and analyzed in MATLAB using a custom written code (coloc_FA, provided in supplemental information as Data S1). An object-based co-localization approach was performed. Concisely, each channel was segmented, and a binary mask generated. The masks were combined and the fraction of pixels with overlapping signals was quantified.

Analysis of adhesion orientation and vinculin-aITGB1 colocalization angle

To analyze FA orientation, high resolution Z-stack confocal images of HUVECs stained for vinculin and aITGB1 were segmented and binarized using ImageJ and then imported and analyzed in MATLAB using a custom written code (coloc_FA, provided in supplemental information as Data S1). An object-based analysis approach was performed. Briefly, each vinculin object orientation was computed to determine FA adhesion orientation. Each vinculin and aITGB1 object centroid coordinated were determined. Each vinculin object was paired to the closest aITGB1 object, and their respective centroids used to determine a vinculin-to-aITGB1 vector. Vector angles were computed to determine the polarization of aITGB1 related to vinculin.

Vessel and endothelial density analysis

For radial expansion quantification, images were taken using an EC Plan-Neofluar, NA 0.30, air 10x objective, in a confocal Laser Point-Scanning Microscope 880 (Zeiss). The migratory length of the vascular plexus was analyzed by measuring the total length of the retinal vasculature from the optic nerve, in the center, towards the retinal periphery – sprouting front.

For the quantification of the number of tip cells, tile-scan images of the whole sprouting front were taken with a C-Apochromat Corr, NA 1.20, water 40x objective in a confocal Laser Point-Scanning Microscope 880 (Zeiss). The number of tip cells was then counted, and the values normalized by the sprouting front length.

Regarding vessel density, tile-scan images of the whole petal were acquired using a Plan-Apochromat, NA 0.8, air 20x objective in a confocal Laser Point-Scanning Microscope 880 (Zeiss). After vessel segmentation using FIJI and Photoshop, vessel density was calculated as a ratio between vessel area and total area of the petal.

Endothelial cell density was calculated using 20x tile-scan images acquired in a confocal Laser Point-Scanning Microscope 880 (Zeiss). The number of ERG^+ nuclei counted manually was normalized by the vascularized area for each petal (two petals for each retina).

Vascular morphogenesis parameters and principal component analysis

Retinal vascular plexuses were imaged, binarized, and skeletonized following the protocol previously described in Bernabeu et al. (2018). Vessel diameter was stored as a node attribute in the graph data structure. Plexus Morphometrics were calculated using a MATLAB script developed in this study (https://doi.org/10.5281/zenodo.7036288). In detail, the resulting planar graphs were manually cropped to the arterial region of interest and simplified by merging edges that met at nodes of degree 2. Every remaining vertex in the graph was therefore a bifurcation (degree 3), the tip of blind-ended vessel (sprout or vessel undergoing pruning) (degree 1) or vessel leaving the region of interest (degree 1). The faces of the planar graph were obtained, and their area calculated. The sprouting front boundary was defined as the line connecting the tips of the two sprouts protruding the most in the sprouting front. With this line as reference, the following graph properties were calculated in bins of 100 μm width moving away from the sprouting front: vessel density (number of graph edges per unit of vascularized area in the bin), bifurcation density (number of degree 3 nodes per unit of vascularized area in the bin), range of avascular areas (difference between maximum and minimum area of the faces calculated in the bin), mean avascular area (mean of the distribution of face areas in the bin), standard deviation of avascular areas (standard deviation of the distribution of face areas in the bin), mean diameter (mean of the distribution of vessel diameters in the bin), and standard deviation of diameters (standard deviation of the distribution of vessel diameters in the bin). Principal component analysis (PCA) decomposition of the 7-dimensional vectors defining the previous features at each bin in each control retina was performed to facilitate visualization and bin classification based on phenotypic similarity. Weights were as following: PCA1 [-0.453; -0.345; 0.348; 0.366; 0.404; -0.406; -0.304]; PCA2 [0.346; 0.0638; 0.523; 0.220; 0.491; 0.423; 0.366], for vessel density; bifurcation density; range of avascular areas; mean avascular area; standard deviation of avascular areas; mean diameter; and standard deviation of diameters, respectively. The k-means clustering algorithm was used to find two clusters that minimize within cluster variance under the assumption that two main phenotypic classes (sprouting and remodeling) exist. The PCA decomposition of the control group was used to map the bins of the remaining groups to the same phenotypic space. The k-means classifier was used to classify these bins according to their distance to the center of the sprouting/remodeling clusters in the control group.

Polarity index quantifications *in vitro*

To quantify cell polarity, tile-scan images of HUVECs stained for Golgi (Golph4) and nuclei (DAPI) markers were processed in FIJI. Afterwards, each set of images was imported and analyzed in MATLAB using a modified version of a polarity analysis script kindly provided by Anne-Clémence Vion and Holger Gerhardt (PI_calculator, provided in supplemental information as Data S2).

Briefly, after segmenting each channel corresponding to the Golgi and nuclear staining, the centroid of each organelle was determined and a vector connecting the center of the nucleus to the center of its corresponding Golgi apparatus was drawn. The Golgi-nucleus assignment was done automatically minimizing the distance between all the possible couples. The polarity of each cell was defined as the angle between the vector and the slide axis. An angular histogram showing the angle distribution was

then generated. Circular statistics were performed using the Circular Statistic Toolbox. The polarity index (PI) was calculated as the length of mean resultant vector for a given angular distribution.

$$polarity\ index = \sqrt{\left(\frac{1}{N}\sum_{1}^{N}\cos\alpha\right)^2 + \left(\frac{1}{N}\sum_{1}^{N}\sin\alpha\right)^2}$$

The PI varies between 0 and 1. The closer to 1, the more the data are concentrated around the mean direction, while values close to 0 correspond to random distribution. PI indicates the collective orientation strength of the cell monolayer. Box plots were generated by using every single PI calculated for images of each biological replica, which show the biological variability of the system. This data was used to calculate the significance of differences between experimental conditions.

Flow and chemoattractant polarity indexes in retinas

In the *in vivo* polarity analysis, we quantified polarity and correlated it with blood flow direction by using the approach described in Bernabeu et al. (2018). Briefly, all the retinal vascular plexuses were imaged in a Zeiss Cell Observer SD (Zeiss) equipped with Zen software and with a Plan-Apochromat 40x NA 1.40 oil objective and post-processed to generate a binary mask from the ICAM2 channel and a second image with at least the ERG (EC nuclei) and Golph4 (Golgi apparatus) channels. These two images defined the input to PolNet. PolNet is a graphical user interface that allows the user to perform three tasks: 1) to construct a flow model from the ICAM2 mask and use the HemeLB flow solver to estimate the wall shear stress across the whole network (as well as blood velocity, shear rate, and pressure); 2) to draw cell polarity vectors (nuclei to Golgi) for each endothelial cell in the network based on the Erg-Golph4 image; and 3) to statistically analyze the relationship between the cell polarity and flow direction or wall shear stress.

Chemoattractant (K-) and Flow (F-) polarity indexes were then calculated using the angle that each Nuclei-to-Golgi vector does with either the sprouting front edge (K-), defined as a line between the two most outward vascular sprouts, or the flow direction (F-) using the length of mean resultant vector for a given angular distribution, as previously described (Bernabeu et al., 2018; Carvalho et al., 2019; Franco et al., 2015, 2016). The K- and F-indexes were calculated using 3 consecutive Matlab scripts generated in the lab (AnalysisSubRegion_Scale, Merge_Regions and Merge_All, all provided in supplemental information as Data S3). (The polarity index varies between -1 (backward polarization – away from the sprouting front, if K-index; or with the flow direction, if F-index) to 1 (forward polarization – towards free edge of the sprouting front, if K-index; or against the flow direction, if F-index), where 0 means random polarization. Chemoattractant (K-) and Flow (F-) polarity indexes were then represented as a function of the distance from the sprouting front (SF) to the optic nerve (ON).

Statistical analysis

All statistical analysis was performed using GraphPad Prism 7. Measurements were taken from distinct samples, and statistical details of experiments are reported in the figures and figure legends. Sample size is reported in the figure legends and no statistical test was used to determine sample size. The biological replicate is defined as the number of cells, images, animals, as stated in the figure legends. No inclusion/exclusion or randomization criteria were used and all analyzed samples are included. Normality tests were performed to assess the data normality. Comparisons between two experimental groups were analyzed with two-sided unpaired parametric t test or Mann-Whitney test depending on the data normality. Multiple comparisons between more than two experimental groups were assessed with one-way ANOVA. We considered a result significant when $p<0.05$. For all box plots: centerline, median; +, mean; whiskers, min to max.